Interaction of Vortex Streets with a Downstream Wing

Burak Turhan, Zhijin Wang, Ismet Gursul

University of Bath, UK

The unsteady aerodynamics of a wing in the wake of a periodically plunging upstream airfoil was investigated in water tunnel experiments. By varying the frequency and the amplitude of the plunge oscillations, vortex-street configurations with varying wavelength and circulation were generated. Depending on the angle of attack of the wing, the largest lift force is found when the leading-edge of the wing is located at the wake centerline or just above it. Flow separation at the leading-edge, formation of a leading-edge vortex, and coupling with incident vortices are observed with increasing angle of attack. The lift time history has higher harmonics up to $n = 5$ when the wing is close to the wake centerline. This is due to the cross-stream velocity profile in the undisturbed wake and can be also predicted by a point vortex model. The peak lift coefficients decrease with increasing deflection angle of the wake if the upstream airfoil is plunged at nonzero mean angle of attack. This occurs as the geometry and circulations of the vortices in the reversed Karman vortex street are modified. For the unloaded wing in the symmetric wakes, the peak lift coefficients increase with increasing frequency and amplitude of the plunging airfoil. These kinematic parameters also determine the amplitude and shape of the cross-stream velocity profiles and the degree of two dimensionality in the undisturbed wake. The amplitude of the lift coefficient of the wing depends on a single wake parameter, which is the Strouhal number based on the amplitude of the upstream airfoil.

I. INTRODUCTION

The interaction of rows of vortices originated from separated shear layers, two-stream mixing layers, and bluff-body wakes with downstream bodies was reviewed by Rockwell [1]. The class of parallel vortex street-body interactions can be observed for wings in the wakes of stationary and oscillating upstream bodies. The interaction of the Karman vortex street of a stationary upstream body with a downstream elliptical-edge was investigated by Gursul and Rockwell [2]. Depending on the circulation, wavelength, and the offset distance from the body, the interaction and the distortion of the incident vortices produce different unsteady pressure fields. Recent investigations on the aerodynamics of wings in bluff-body wakes [3-5] revealed significant effects on the unsteady as well as time-averaged forces. Relevant applications of this type of vortex street interactions are found in the aerodynamics of tandem wings, formation flight, flight refuelling, and wings in ship airwakes.

It was demonstrated that it would be possible to exploit the energy of the vortex streets for flexible [6] or oscillating bodies [7]. The unsteady wings in the wakes of upstream bodies have applications in energy harvesting [6], formation flight of birds [8], unsteady aerodynamics of dragonflies [9,10], and oscillating tandem foils [11]. In this class of flows, it is known that the arrival time of the incident vortices with respect to the wing motion is critical.

In this study we focus on a stationary wing in the wake of a plunging airfoil. It is known that, with increasing Strouhal number of airfoil oscillations, the Karman vortex street with net drag force switches to a reverse Karman vortex street with net thrust force. This canonical flow is highly relevant to the vortex-body interactions [1], formation flight of birds and flapping-wing micro air vehicles [8,12], and even for fixed-wing vehicles encountering gusts and turbulence [13]. By varying the frequency and the amplitude of the airfoil plunging motion to generate the unsteady wake, the circulation and the wavelength can be altered to some extent. In a broader view, the oscillating wake of a plunging airfoil represents “periodic travelling gusts” that have finite cross-stream length scale. We note that the spanwise length scale (two-dimensionality of the flow) is dependent on a single parameter, the Strouhal number [14].

Historically, periodic travelling gusts in the experimental facilities were generated by oscillating airfoils or cascade of airfoils [15-21], and by oscillating flaps [22,23]. Comparisons between the force measurements and the theoretical predictions using the Sears function were made when the gust cross-stream length scale was large compared to the airfoil dimensions. (In

the Sears formulation, the gust amplitude is constant in the cross-stream direction). The unsteady wakes of plunging airfoils represent more realistic gusts with large but localized velocity fluctuations, for which the cross-stream and the spanwise length scales depend on the kinematic parameters for the oscillating airfoil. Comparison of large amplitude airfoil motions or gust encounters with the small-amplitude linear theory was also made. For example, Chiereghin *et al.* [24] found reasonable agreement with the linear theory for large amplitude plunging motion. Motivated by their findings, we have also compared the results of the present experiments with the Sears theory.

In this paper, we investigate the interaction of unsteady wake of a periodically plunging airfoil with a stationary downstream wing at a chord Reynolds number of Re = 20,000 by means of particle image velocimetry (PIV) and lift force measurements. First, we characterize the incident wake generated by the plunging airfoil by means of two-point cross-correlations and phase-averaged flow fields, while the kinematic parameters (frequency and amplitude) are varied. Then we investigate the interaction of the wakes with a wing by means of unsteady lift measurements, phase-averaged vorticity fields, and the Proper Orthogonal Decomposition (POD). Finally, we report the effects of the kinematic parameters on the interaction and the lift force.

II. METHODS AND TECHNIQUES

A. Experimental setup

The experiments were performed in a closed-loop, free surface water tunnel (Eidetics model 1520) at the University of Bath. This facility can provide a maximum freestream velocity of 0.5 m/s, with a turbulent intensity of around 0.5% [25]. The main test section of the facility is 381 mm wide, 508 mm deep, and 1520 mm long, and tempered glass is used in the test section for the camera and laser access. Figure 1 gives a basic overview of the side and front views of the test section, the plunging mechanism, the support structure of the downstream wing, and the schematic of the PIV setup.

Both the airfoil and the finite downstream wing were mounted vertically with respect to the tunnel and the freestream velocity. The NACA0012 profile was used for both the airfoil and the wing. The chord length of the upstream airfoil was c = 62.7 mm, with an aspect ratio of AR = 5, but represented an airfoil as the end-plates were used at both ends. The downstream wing had a

chord length of c = 62.7 mm and a semi-aspect ratio of sAR = 3. The coordinate system was located at the root of the upstream airfoil and at the trailing-edge as sketched in Figure 1. Both the airfoil and the wing were manufactured by selective laser sintering using Polyamide (PA) 2200, with a smooth finish and subsequently spray-painted matte black to eliminate laser reflection during visualization. To provide spanwise stiffness, a T800 carbon fibre inset was slotted along the spanwise direction for the models. The long end-plate placed near the root of the airfoil prevented any free surface effects. Both end-plates above and below the upstream airfoil, with 2 mm clearance, extend 2c upstream and 10c downstream of the airfoil to obtain nominally two-dimensional flow field. This setup was previously used by Chiereghin *et al*. [24].

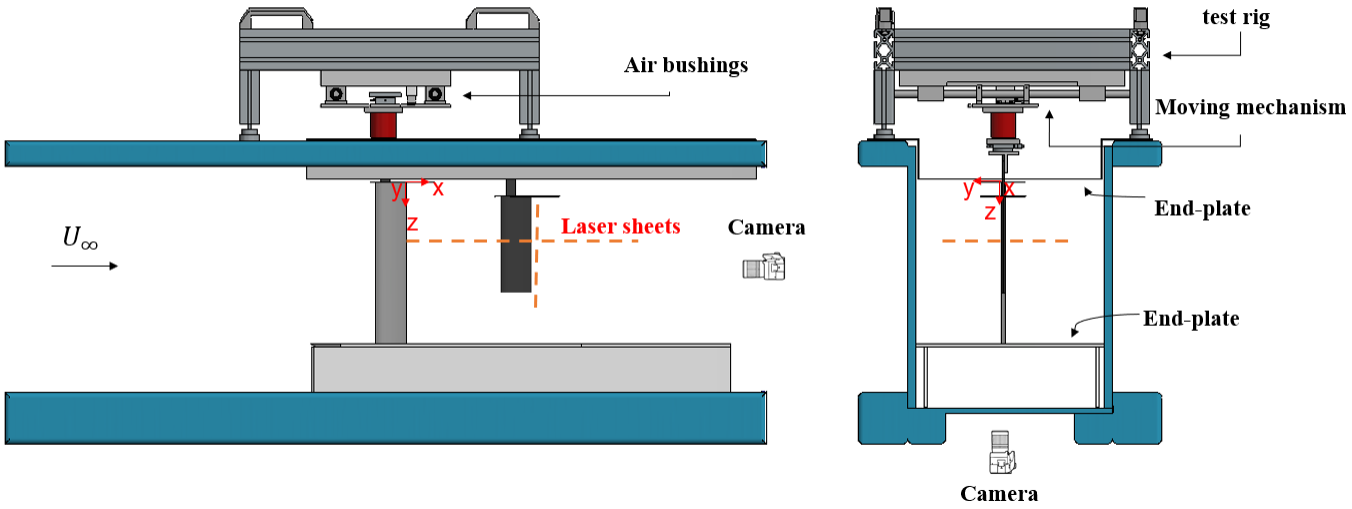

Figure 1 Schematic of the test section and the PIV system.

The plunging rig consisted of a fixed platform, which was placed at the top of the water tunnel test section. The upstream airfoil was connected to the platform through a rotation stage that allowed the airfoil to rotate, thus adjusting the desired geometric angle of attack with an accuracy of ±0.2º. The plunging motion, provided by a Zaber LSQ150B-T3 translation stage, was powered by a stepping motor with an X-MCB1 controller. The plunging motion $h(t)$ of the airfoil displacement in the cross-stream y-direction can be expressed in the form of:

$$h(t) = \frac{A}{2}\cos(2\pi f t) \tag{1}$$

which can be reproduced with an accuracy of 2%. Here the displacement $h(t)$ is measured from the mean location of the airfoil (y = 0). The uncertainty of the velocity of the plunging motion is estimated to be less than 3%.

The downstream wing was mounted to a binocular force balance, and its leading-edge was placed at x/c = 3. In order to avoid the end-wall effects of the incoming unsteady wake on the downstream wing, there was a gap of 0.5c between the airfoil end-plate and the wing end-plate. In addition, to minimize the interference effects of the wing end-plate on the force measurements, we kept the dimensions of the wing end-plate small. The Reynolds number based on the chord length was Re = 20,000. The vortex streets reported in this paper remain parallel to the freestream in the near wake for $\alpha_{airfoil}$ = 0°. The deflected wakes (in the absence of the downstream wing) are observed at much higher plunge velocities as we previously documented in this facility [26].

B. Particle image velocimetry measurements

The experiments were conducted at various plunging reduced frequencies (up to $k = \pi fc/U_\infty$ = 3.14) and normalized peak-to-peak amplitudes (up to A/c = 1), as shown in Figure 2. In this amplitude versus frequency plot, maximum amplitudes and frequencies are limited by the stepping motor, and roughly correspond to a constant value of maximum plunge velocity. Most of the measurements were carried out in the mid-span plane of the wing (z/c = 2) to capture the streamwise flow. In addition, we performed some experiments in the crossflow plane just downstream of the wing (x/c = 4.03) as shown in Figure 1. The crossflow PIV measurements were carried out in an area that covered a region between z/c = 1 and 4. The measurement region is believed to be free of the end-wall effects. Calderon *et al*. [27] measured the influence of the wall boundary layer on the vortical flow in the same facility for a comparable chord length, gap, and Reynolds number, and found that it was restricted to a zone not broader than 0.15c at x/c = 1, which may be used as a reference for our study at x/c = 4.03.

The PIV system is a commercially available TSI system that consists of a synchroniser (TSI model 610036), a double-pulsed laser (Nd: YAG 50mJ), and an 8 MP camera. The time interval between two laser pulses was Δt = 0.8 ms. Commercially available hollow glass spheres (8-12 micron in diameter) were used to seed the water. The images were analysed via algorithms by the TSI's software package INSIGHT 4GTM using Fast Fourier Transform (FFT). The image

processing was done with an interrogation window size of 32 by 32 pixels with 25% overlap, resulting in a spatial resolution of 2.5%c. The primary peak ratio (PPR) algorithm for PIV uncertainty has been implemented and calibrated within INSIGHT 4GTM for each set of PIV processing parameters. The PPR method was used to calculate the instantaneous measurement uncertainty with extended uncertainty within a 95 percent confidence level [28]. The mean uncertainty was approximately 2% of the free stream velocity.

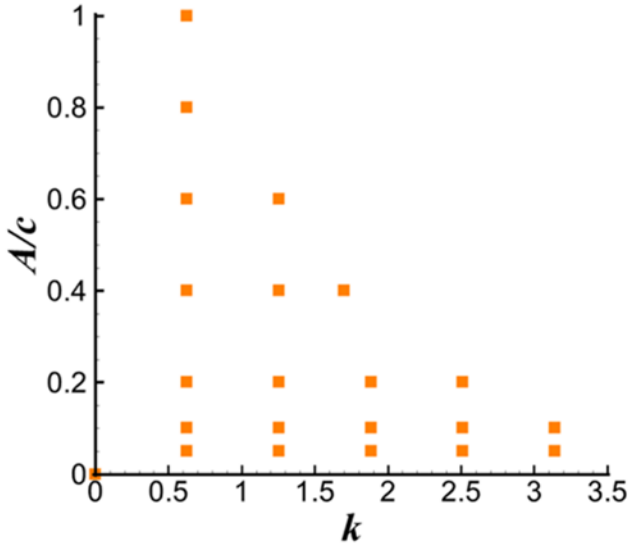

Figure 2 Normalized amplitude versus reduced frequency for the test cases.

We had two types of velocity measurements. For one specific set of the kinematic parameters (k = 1.70 and A/c = 0.4), we obtained phase-locked measurements. The phase-locked data were averaged using 60 image pairs acquired at equal intervals in a plunging period, i.e., at t/T = 0, 0.25, 0.50, and 0.75. For a wide range of frequency and amplitude parameters ($k \leq 3.14$, A/c = 1), we obtained 2,000 sequential instantaneous flow fields with continuous sampling. The data sampling rate was chosen as 3.75 Hz (which was not a subharmonic or higher harmonic of the plunging frequency). The data obtained this way could be processed to obtain the time-averaged data (mean and rms velocity) as well as the two-point cross-correlations and the POD modes.

In this paper, the POD analysis was performed using commercial software TSI GRAD-POD TOOLBOX, which employs the spatial-temporal data analysis technique proposed by Heiland [29]. The cross-stream velocity component can be expressed as:

$$v(x,y,t) = V(x,y) + v'(x,y,t) = V(x,y) + \sum_{1}^{N} a_n(t)\phi_n(x,y) \quad (2)$$

where V is the mean cross-stream velocity component, and v' is the fluctuating cross-stream velocity component of the velocity field. Here ϕ_n and a_n are the POD modes and corresponding mode coefficients. The ratio of the energy of each mode to the total energy has particular importance. The small number of POD modes with most of the energy imply highly coherent flows. We will discuss the energy of the POD modes later in the paper. As previously shown, most of the energy is captured in the first two modes for oscillating wakes of plunging airfoils [14].

Oudheusden *et al*. [30] proposed a phase-averaging method based on the POD analysis for the wake of a bluff body. Their method is based on the fact that the periodic flow due to vortex shedding is dominated by the first two POD modes:

$$v(x,y,t) \approx V(x,y) + a_1(t)\phi_1(x,y) + a_2(t)\phi_2(x,y) \quad (3)$$

where the coefficients a_1 and a_2 are found using the first two eigen-values:

$$a_1 = \sqrt{2\lambda_1}\sin(\varphi)\,, a_2 = \sqrt{2\lambda_2}\cos(\varphi) \quad (4)$$

here φ is the vortex shedding phase angle, assumed to increase linearly with time according to $d\varphi/dt = 2\pi f$, where f is the fundamental frequency of vortex shedding. We have done phase-averaging using a bin size of 10°. For $k = 1.70$ and $A/c = 0.4$, Figure 2 compares the cross-stream velocity field $\langle v \rangle$ in the wake, obtained from the phase-locked (to the airfoil motion) velocity measurements and the POD-based phase-averaged velocity field. The agreement between the two methods is very good. This allowed us to use the POD-based phase-averaging method for a wide range of frequency and amplitude.

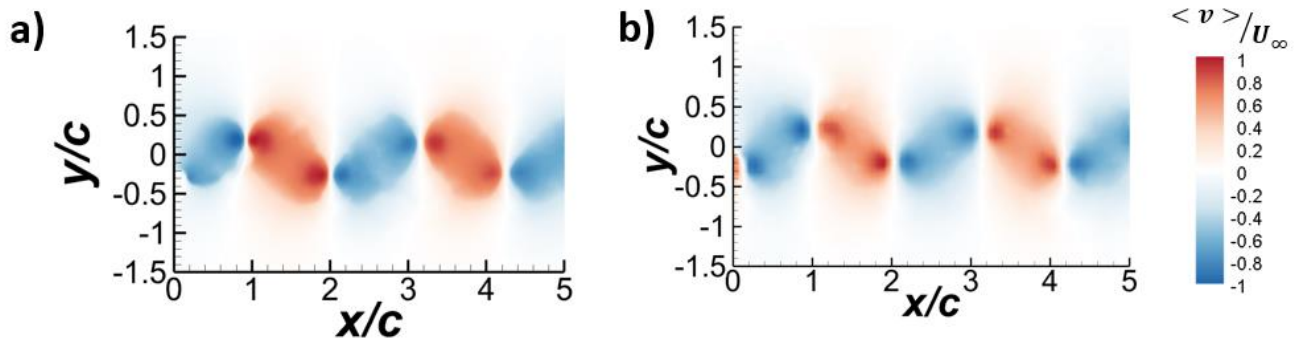

Figure 3 Contour plots of cross-stream velocity for A/c=0.4, k=1.70, at t/T=0.5 a) phase-locked to airfoil motion, b) phase-averaged based on the POD.

C. Force measurements

A binocular strain gauge force balance, which was machined in-house from Aluminium 2014T6, was used to make direct lift force measurements. This type of strain gauge balance is known to be insensitive to the bending moment and has been widely used [31,32]. The binocular load cell was calibrated by a pulley and weights. Voltage signals were amplified through an Analog Devices AD624 amplifier. A digital third-order Butterworth low-pass filter was used in LABVIEW to remove any high-frequency noise above 30 Hz (about k = 18). The lift data for the wing in freestream (in the absence of plunging upstream airfoil) were acquired for 60 seconds at a sampling rate of 1 kHz. When the wing is submerged in the oscillating wake behind the plunging airfoil, an integrated LabVIEW program ensures the synchronisation of the plunging motion and the lift force data. For each case, 60 cycles were recorded, with 2,000 samples per period. The phase-averaged lift force was then calculated.

III. RESULTS AND DISCUSSION

Figure 4a shows the variation of the time-averaged lift coefficient as a function of angle of attack for the downstream wing (sAR = 3) in freestream. We compare our data with those for the same aspect ratio (sAR = 3) [33] as well as for sAR = 2 [34], sAR = 5 [35] and airfoil [24,36], all with the same NACA0012 cross-section and at the same Reynolds number of Re = 20,000. The lift curve slopes according to the lifting line theory are also shown with solid lines. There is good

agreement with the data for the same aspect ratio. The average lift slope decreases with decreasing aspect ratio as expected; however, the nonlinear behaviour of the lift slope is apparent for all wings. The peculiar variation at small angles of attack for the NACA0012 cross-section is typically observed for Re < 30,000 and is well documented in the literature as discussed by Cleaver *et al.* [36]. The static stall of the wings becomes more gradual while the maximum lift coefficient decreases with decreasing aspect ratio. The static stall angle of the present wing (sAR=3) is approximately 11 degrees, which agrees very well with the data of Qian *et al.* [33].

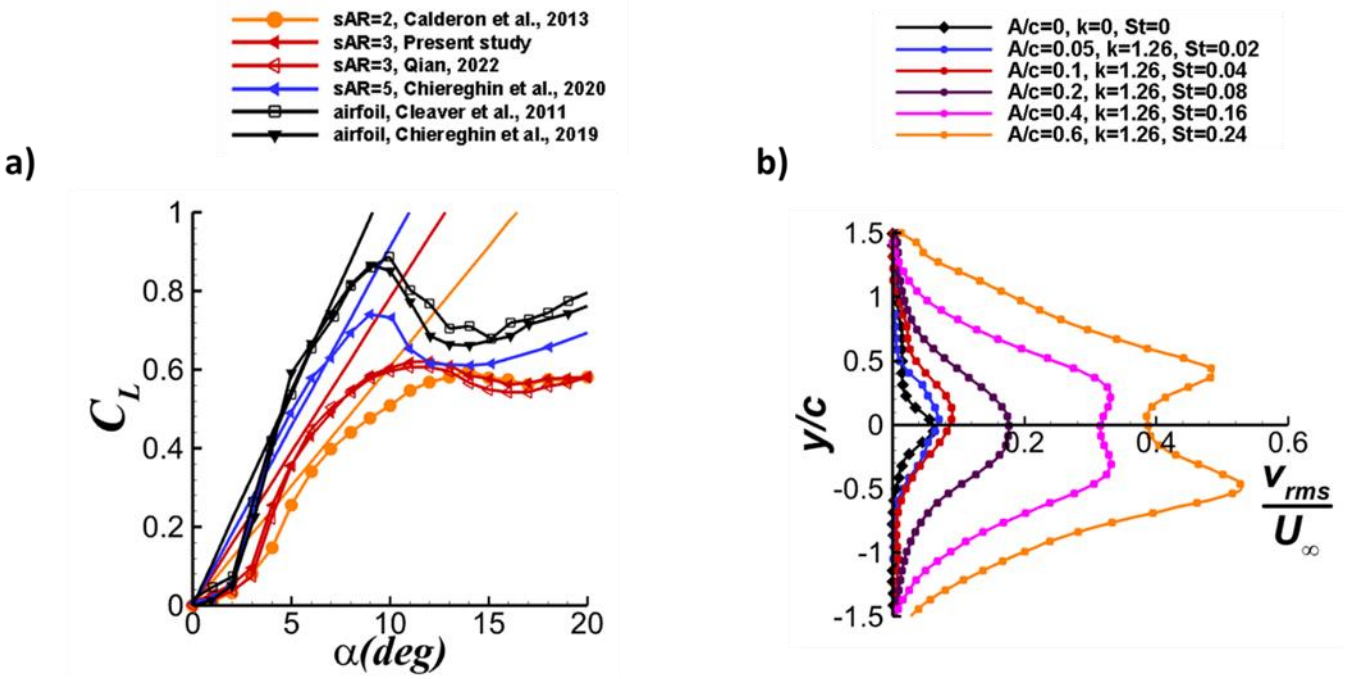

Figure 4 a) Time-averaged lift coefficient in freestream and comparison with literature for stationary NACA0012 wing at the test Reynolds number of Re=20,000; the lift curve slopes according to the lifting line theory are also shown with solid lines; b) rms of cross-stream velocity fluctuations in the incident wake at x/c=4.03 for k=1.26 and various amplitudes.

The sAR = 3 wing was submerged in the oscillating wakes of the upstream plunging airfoil. To give an idea about the magnitude of the velocity fluctuations in the wake in the absence of the wing, we show the variation of the normalized root-mean-square (rms) of the cross-stream velocity fluctuations at x/c = 4.03 for k = 1.26 and various amplitudes in Figure 4b. The chosen reduced frequency is a representative value as it is close to the half of the maximum reduced frequency

tested. In addition, as it is seen in Figure 2, we have five different values of amplitude, whereas with increasing reduced frequency we have less data points to compare. The rms cross-stream velocity fluctuations have a maximum at the wake centerline for small amplitudes ($A/c \leq 0.2$). The double peaks are observed with increasing amplitude ($A/c \geq 0.4$). Large velocity fluctuations with increasing frequency and amplitude are typical in the incident wake, which suggest a collapse of the data with the Strouhal number $St = fA/U_\infty$ (where A is the peak-to-peak amplitude of the plunging oscillations). This will be presented later in the paper. The large velocity fluctuations push the interaction with the wing beyond the small-amplitude potential flow theory. In the next section, we characterize the unsteady wake using various parameters and methods.

A. Characterization of incident wake

Figure 5 shows contour plots of the cross-correlation of the cross-stream velocity component C_{vv} (Figure 5a) and vorticity component $C_{\omega\omega}$ (Figure 5b), as well as the first two most energetic POD modes (Figure 5c) for A/c = 0.4, k = 1.70. Here, the two-point cross-correlation of the cross-stream velocity components is defined as:

$$C_{vv} = \frac{\overline{v'_A v'_B}}{\sqrt{\overline{v'_A{}^2}}\sqrt{\overline{v'_B{}^2}}} \tag{5}$$

where v'_A is the fluctuating cross-stream velocity component at the reference point A, and v'_B is the fluctuating cross-stream velocity component at any arbitrary location B in the measurement domain. The reference point was chosen as x/c=0.5, y/c=0. The wavelength λ of the vortex street can be easily determined from the two-point cross-correlation contours in the streamwise direction. Figure 5b presents the two-points cross-correlation of the vorticity fluctuations in the measurement domain calculated as:

$$C_{\omega\omega} = \frac{\overline{\omega'_A \omega'_B}}{\sqrt{\overline{\omega'_A{}^2}}\sqrt{\overline{\omega'_B{}^2}}} \tag{6}$$

where ω'_A is the fluctuating vorticity component at the reference point A, and ω'_B is the fluctuating vorticity component at any arbitrary location B in the measurement domain. The reference point was chosen as x/c=0.5 and y/c at which the ω_{rms} is maximum. The cross-correlation coefficient $C_{\omega\omega}$ shows vortex street arrangement with the row of positive vortices at the top with

positive $C_{\omega\omega}$ values, and the row of negative vortices at the bottom with negative $C_{\omega\omega}$ values. The spacing b between the rows can be found from this plot. The parameters λ and b for varying frequency and amplitude will be presented later.

Figure 5c presents the first two dominant POD modes of the cross-stream velocity component normalized by its maximum value for the corresponding case. We name these two modes "fundamental wake modes" because they characterize the travelling wave in the wake and correspond to the fundamental frequency. Note that the second mode is shifted quarter-wavelength with respect to the first mode. In this example, the first two most energetic modes have 34.2% and 32.5% of the total energy, hence the wake modes representing large scale vortices travelling downstream have 66.7% of the total energy. In this paper, we will present the energy fraction of the wake modes for the incident wake as well as for the interaction.

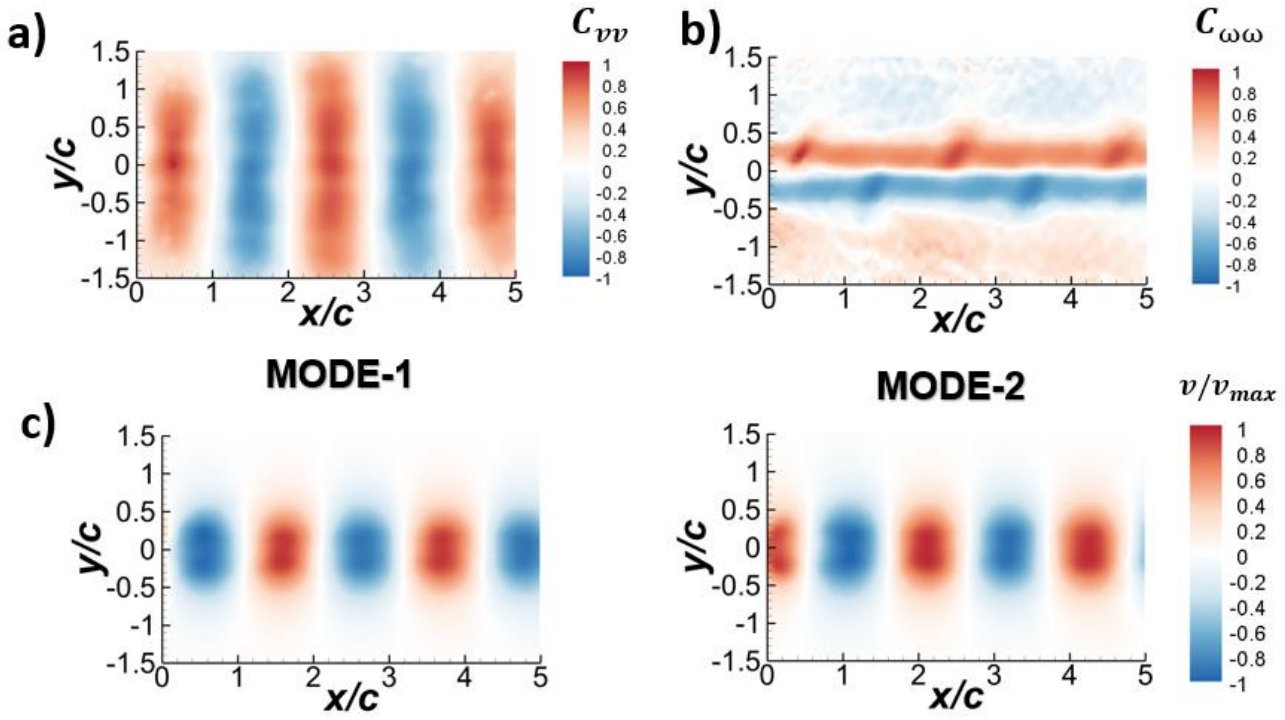

Figure 5 Contour plots of a) cross-correlation of cross-stream velocity component C_{vv}, b) cross-correlation of vorticity component $C_{\omega\omega}$, c) the first two POD modes of cross-velocity component (with fraction of energy of 34.2% and 32.5%); A/c=0.4, k=1.70.

Figure 6 shows the wavelength normalized by the chord length (Figure 6a) and the spacing between the rows (see the inset) normalized by the wavelength (Figure 6b) as a function of the

reduced frequency k. The normalized wavelength λ/c shows remarkable collapse with the reduced frequency for different amplitudes A/c. The dashed line in Figure 6a corresponds to $f\,\lambda = U_\infty$, which implies that the convection speed of the travelling waves is approximately equal to the freestream velocity. In Figure 6b, the data for b/λ do not collapse with the reduced frequency k, however, b/λ increases with k for a fixed value of A/c. We note that the spacing between the rows b cannot be accurately calculated from the two-point cross-correlations of vorticity at low reduced frequencies, and we omitted these data in Figure 6b.

In Figure 6c, the variation of the maximum value of the phase-averaged cross-stream velocity at $x/c = 3$ is shown as a function of the reduced frequency k for the incident wake (in the absence of the downstream wing). This streamwise location is the location of the leading-edge of the wing when the wing is placed in the wake. The same quantity is plotted as a function of the Strouhal number $St = fA/U_\infty$ in Figure 6d. There is a trend of increasing maximum cross-stream velocity fluctuations with increasing k and A/c, however, a large scatter exists. In contrast, the data show much better collapse with St. There is a trend of the data increasing almost linearly with St. As the Strouhal number is the ratio of the maximum plunge velocity of the airfoil to the freestream velocity, it represents the amplitude parameter for the oscillating wake. This was recently shown for the same Reynolds number in the same facility for $x/c \leq 4$ [14]. In Figures 6c and 6d, note that the largest cross-stream velocity component $\langle v \rangle$ is obtained at $A/c = 0.4$, $k = 1.70$, $St = 0.22$ within the range of parameters tested. Consequently, we selected this case as a wake containing intense vortices with large velocity fluctuations and finite length-scale and investigated its interaction with loaded and unloaded wings.

B. Unloaded wing in the wake

In this section we focus on the case of the wing set at an angle of attack $\alpha_{wing} = 0°$. The wake parameters are $A/c = 0.4$, $k = 1.70$, and $St = 0.22$. We also set the upstream plunging airfoil at the mean angle of attack of $\alpha_{airfoil} = 0°$ to produce symmetrically generated wakes. The interaction of the wakes with the downstream wing is discussed as the offset distance between the wing and wake is varied.

Figure 7a-7d show the vorticity contours superimposed on the streamlines at the same phase of the wake (t/T=0.5) for various distances between the wake centerline ($y = 0$) and the wing leading-edge y_{LE}. The corresponding lift coefficient history is presented in Figure 7e. For all four

cases of y_{LE}, there is a counter-clockwise vortex at this phase (t/T = 0.5) either just upstream of the leading-edge or strongly interacting with the wing leading-edge. For closer interactions, there is a slight deflection in the initially horizontal wake axis in addition to some distortion of the classical reverse Karman street configuration. The lift history in Figure 7e shows that there is a local maximum at this phase for y_{LE}/c = 0.8. This is similar to the finding for a single vortex approaching the wing [37]. In contrast, for the other three cases for which the wing is closer to the wake centerline, there is a local minimum in between the two local maximums at this phase.

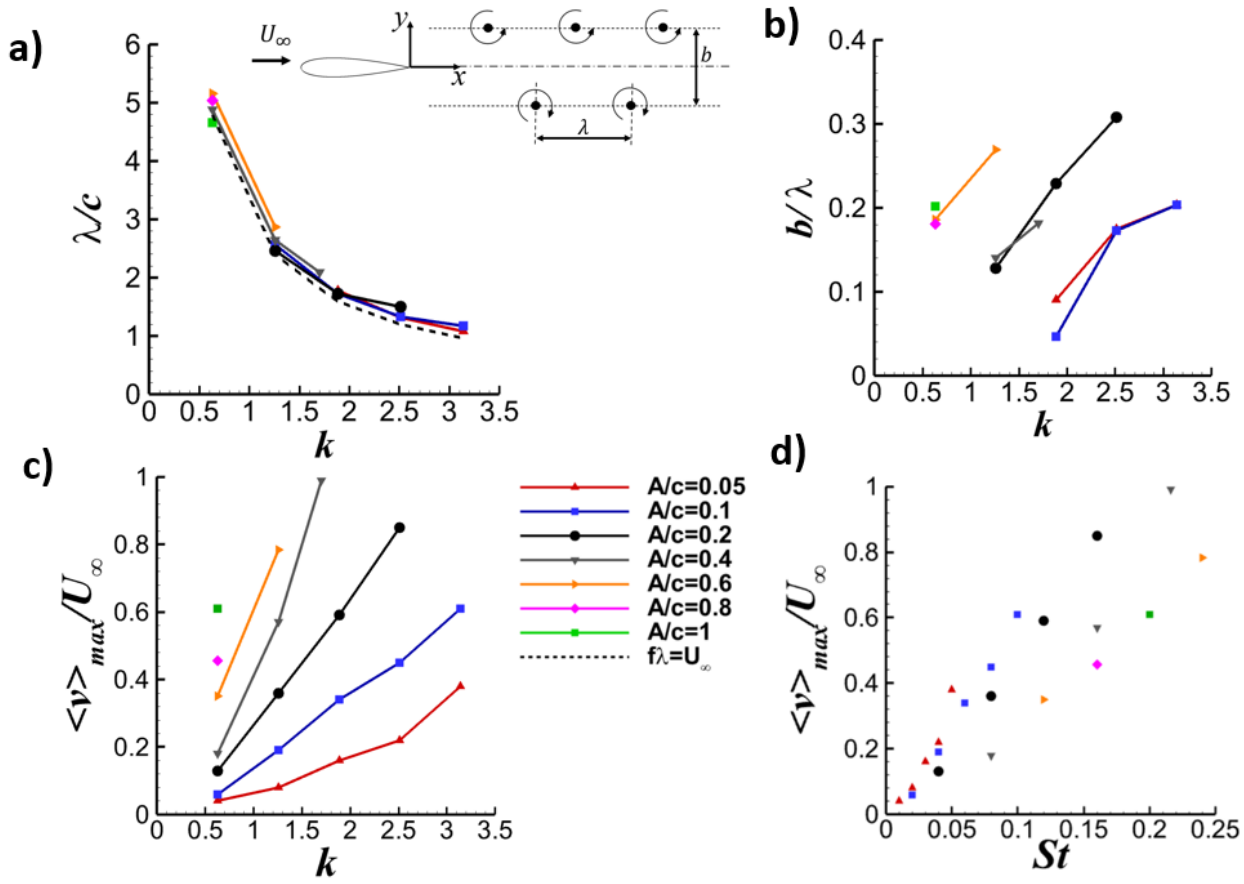

Figure 6 a) Wavelength normalized by chord length as a function of reduced frequency *k*; b) ratio of spacing between rows to the wavelength as function of reduced frequency *k*; (c) and (d) maximum phase-averaged cross-stream velocity normalized by the freestream velocity as a function of reduced frequency and the Strouhal number respectively.

In Figure 8a and 8b we compare the cases of $y_{LE}/c = 0.8$ and $y_{LE}/c = 0$ at four phases. For the case of $y_{LE}/c = 0.8$, as the counter-clockwise vortex approaches the wing the magnitude of the induced velocity is expected to increase. On the other hand, the vertical component decreases until the vortex is just below the wing. Overall, the measured lift history is as expected, and the

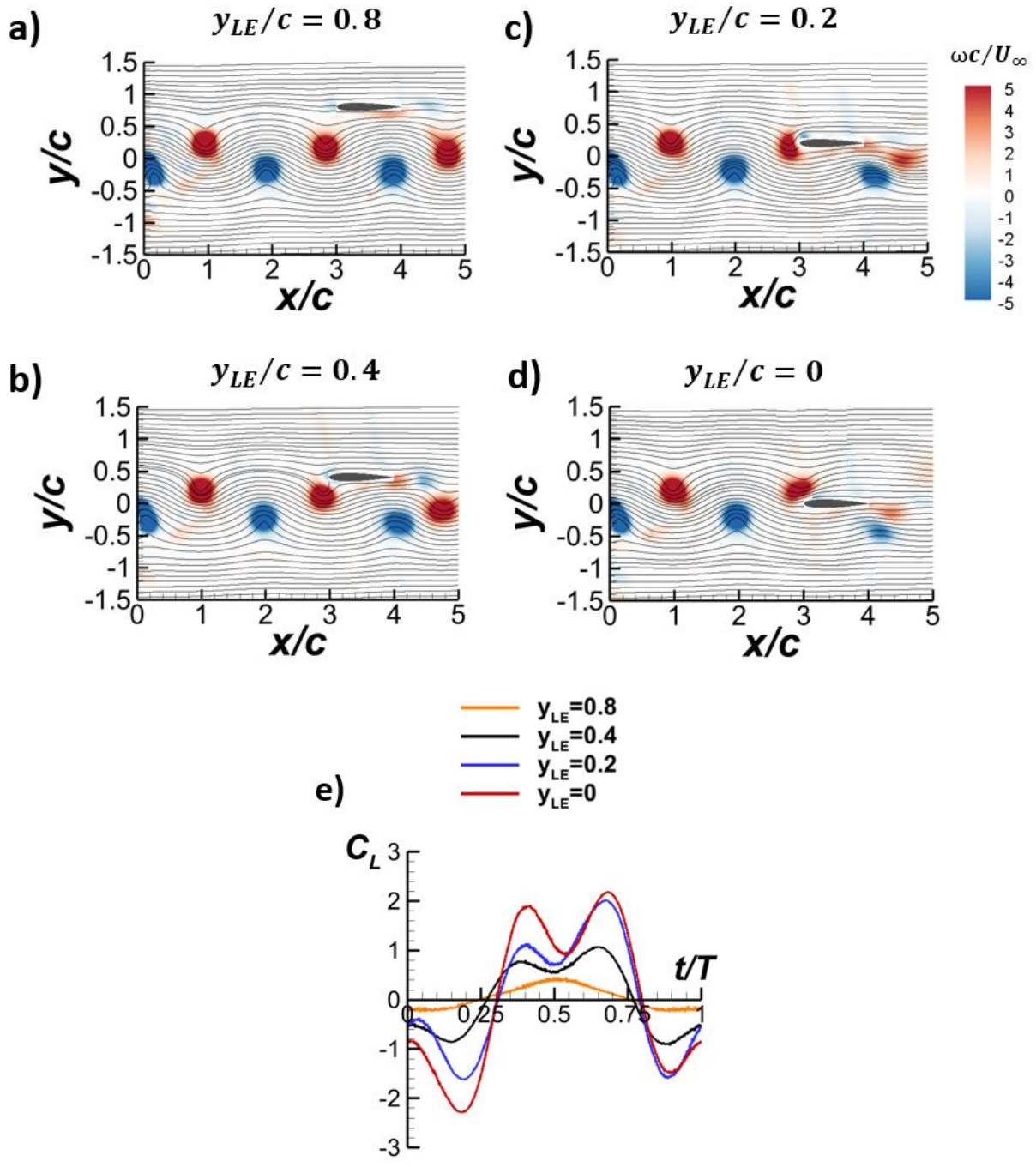

Figure 7 Vorticity contours with streamlines at phase, *t/T*=0.5, for a) $y_{LE}/c = 0.8$, b) $y_{LE}/c = 0.4$, c) $y_{LE}/c = 0.2$, d) $y_{LE}/c = 0$, e) time history of phase-averaged lift coefficient in one cycle, *A/c*=0.4, *k*=1.70, *St*=0.22.

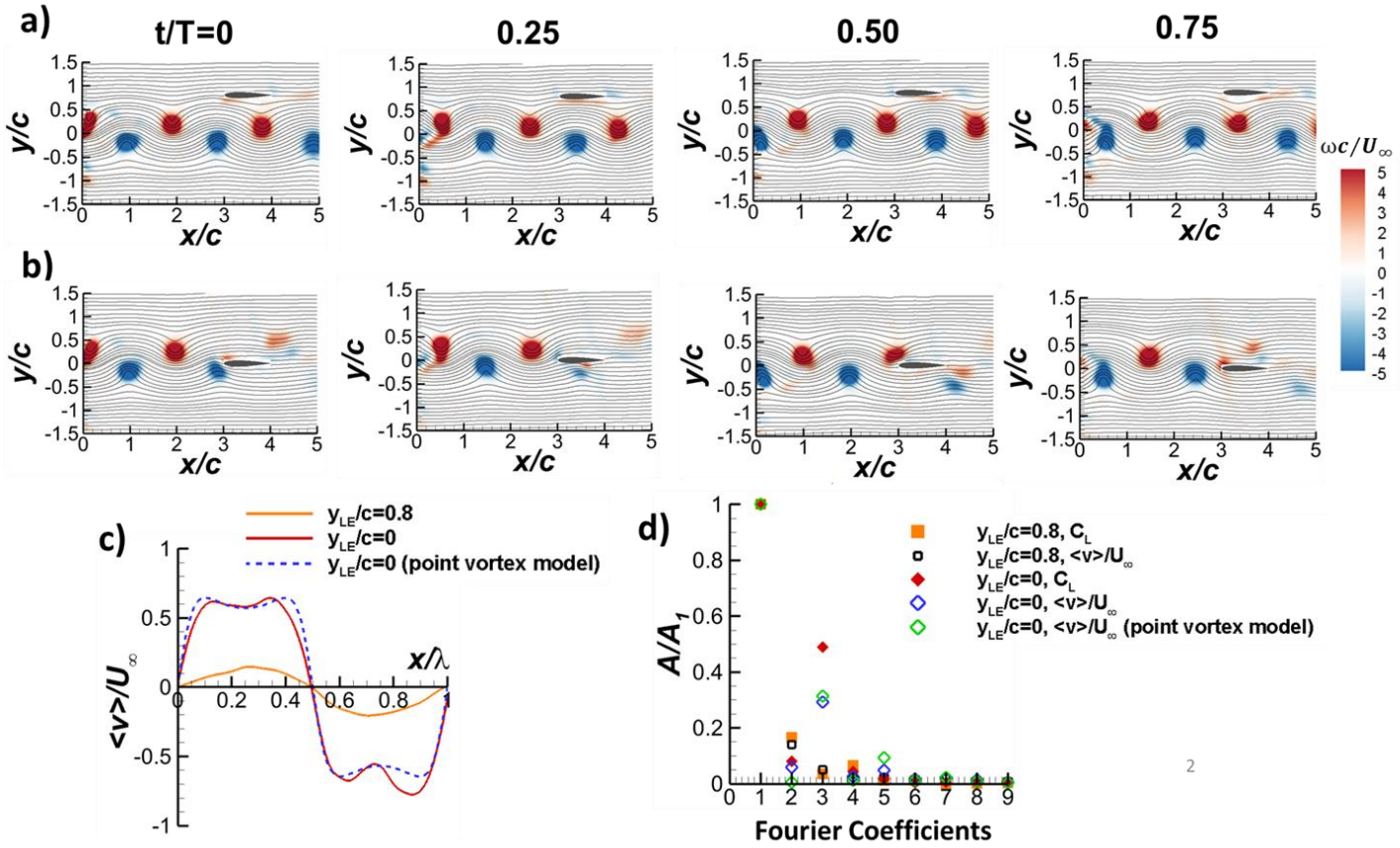

Figure 8 Vorticity contours with streamlines at four phases for a) $y_{LE}/c = 0.8$, b) $y_{LE}/c = 0$, c) cross-stream velocity profile over a wavelength upstream of the wing, d) normalized Fourier coefficients of lift and cross-stream velocity profiles, A/c=0.4, k=1.70, St=0.22.

fundamental frequency is dominant in Figure 7e. However, for the close interaction case for $y_{LE}/c = 0$, the two rows of the vortices make it difficult to have a similar analogy. Even if we focus on a part when the counter-clockwise vortex approaches the wing between t/T = 0.25 and 0.50, the positive peak occurs at an instant between these two phases (see Figure 7e).

In Figure 8c we plotted the cross-stream component of the velocity along the lines of $y_{LE}/c = 0$ and $y_{LE}/c = 0.8$ in the undisturbed wake upstream of the wing over a wavelength. Here x/λ = 0 and 1.0 correspond to the locations of the counter-clockwise vortices (just below or just above the core of the vortices). These spatial profiles of the cross-stream component over a wavelength can be considered as the "gust" profiles upstream of the wing. Not only the two cases differ in magnitude, but also appear to have different waveforms. The case of $y_{LE}/c = 0$ has

clearly higher harmonics. This case appears to be closer to a square-wave rather than a sine-wave. This is further illustrated in Figure 8d, where the Fourier coefficients normalized by that of the fundamental frequency are plotted for the measured upstream cross-stream profile and measured lift coefficient. Both these quantities exhibit strong 3rd harmonic for the close interaction case ($y_{LE}/c = 0$). As the third harmonic also existed upstream of the wing, we conclude that the double peaks in the lift coefficient are not due to the distortion of the vortices as they interact with the wing.

We considered a point vortex model of the reverse Karman street to model the wake [7]. In the undisturbed vortex street along the wake centerline, the velocity components can be calculated from

$$[u - iv]_{y=0} = U_\infty + \frac{i\Gamma}{\lambda}\frac{\cos h\left(\frac{\pi b}{\lambda}\right)}{\sin\left(\frac{2\pi x}{\lambda}\right) - i\sinh\left(\frac{\pi b}{\lambda}\right)} \tag{7}$$

where $i^2 = -1$, and Γ is the circulation of the vortices. The cross-stream velocity component along the wake centerline can be written as:

$$[v]_{y=0} = -\frac{\Gamma}{\lambda}\cosh\left(\frac{\pi b}{\lambda}\right)\frac{\sin\left(\frac{2\pi x}{\lambda}\right)}{\left(\sin\left(\frac{2\pi x}{\lambda}\right)\right)^2 + \left(\sinh\left(\frac{\pi b}{\lambda}\right)\right)^2} \tag{8}$$

In this equation we are only interested in $[v]_{y=0}$ as a function of (x/λ) to be able to compare with the experiments. The first term containing $\frac{\Gamma}{\lambda}\cosh\left(\frac{\pi b}{\lambda}\right)$ has no effect on the function of (x/λ). Although we have calculated λ using the cross-correlations, it is not always possible to calculate b accurately using the cross-correlations of vorticity as it becomes very small at low reduced frequencies as noted previously. In addition, we have not attempted to calculate the circulation Γ for all cases as this brings new challenges (area of vortex, integration of vorticity or velocity, and decreasing coherence of the flow with decreasing Strouhal number – meaning that phase-averaged flow does not accurately represent the flow). Instead, we compare the functional dependence of $[v]_{y=0}$ on x/λ with experiments by adjusting the value of $\frac{\Gamma}{\lambda}\cosh\left(\frac{\pi b}{\lambda}\right)$.

In Figure 8c we plotted the variation of $[v]_{y=0}$ after the adjustment to have a comparison with the experimental data. It is remarkable that the point vortex model also predicts the existence of the double peaks in Figure 8c and the third harmonic in Figure 8d. Hence, we conclude that neither the finite core size of the vortices nor their distortion during the interaction is responsible for the multiple peaks observed in the lift history. We note that Equation (8) also predicts that the variation of the cross-stream velocity along the centerline in the undisturbed wake primarily depends on the vortex array aspect ratio b/λ. This parameter is a strong function of the reduced frequency k and the normalized amplitude of the plunging motion A/c as shown in Figure 6b. We will return to Equation (8) when we discuss the effects of the reduced frequency and the oscillation amplitude on the measured lift response later in the paper.

As noted earlier, the unsteady wake represents a travelling gust with finite cross-stream length scale. The POD modes of the cross-stream velocity component help to visualize the interaction with the wing. Figure 9 presents the first two dominant POD modes of the cross-stream velocity component for $y_{LE}/c = 0.4$ representing a case with weaker interaction and $y_{LE}/c = 0$ for the direct collision. The cross-stream velocity component represents the "gust" velocity and may be easier to relate to the unsteady lift in this case. The POD modes of the cross-stream velocity not only provide the length scales in the streamwise and cross-stream directions, but also the energy fraction of the dominant modes. In Figure 9, the amplitude of the POD modes of the cross-stream velocity is maximum at the wake centerline and covers a region that spans nearly one chord length in the vertical direction. Again, the first two modes have nearly equal energy percentages. The sum of the first two modes (the wake modes) has 51.2% for the weaker interaction and 50.2% for the direct collision in the same measurement domain, which represents slight decrease compared to the undisturbed wake (66.7% discussed in relation to Figure 5). As for the two cases in Figure 9 there is very little change in the energy of the wake modes, we conclude that the effect of the offset distance between the wing and the wake centerline is minor in terms of the wake coherence.

Figure 10 presents the maximum and minimum phase-averaged lift coefficients as a function of the offset distance (the location of wing leading-edge y_{LE}). There is slight asymmetry in the distribution of the peak lift coefficients with respect to the wing offset. This could be due to a micro misalignment of the wing with the wake centerline. In addition to the maximum and minimum values, the time-averaged lift coefficient is shown with dashed lines, but this is not

visible as it is nearly zero. As expected, the largest peak-to-peak lift oscillations occur for the direct collision ($y_{LE}/c = 0$). This is similar to the structure of the dominant POD modes in the cross-stream direction.

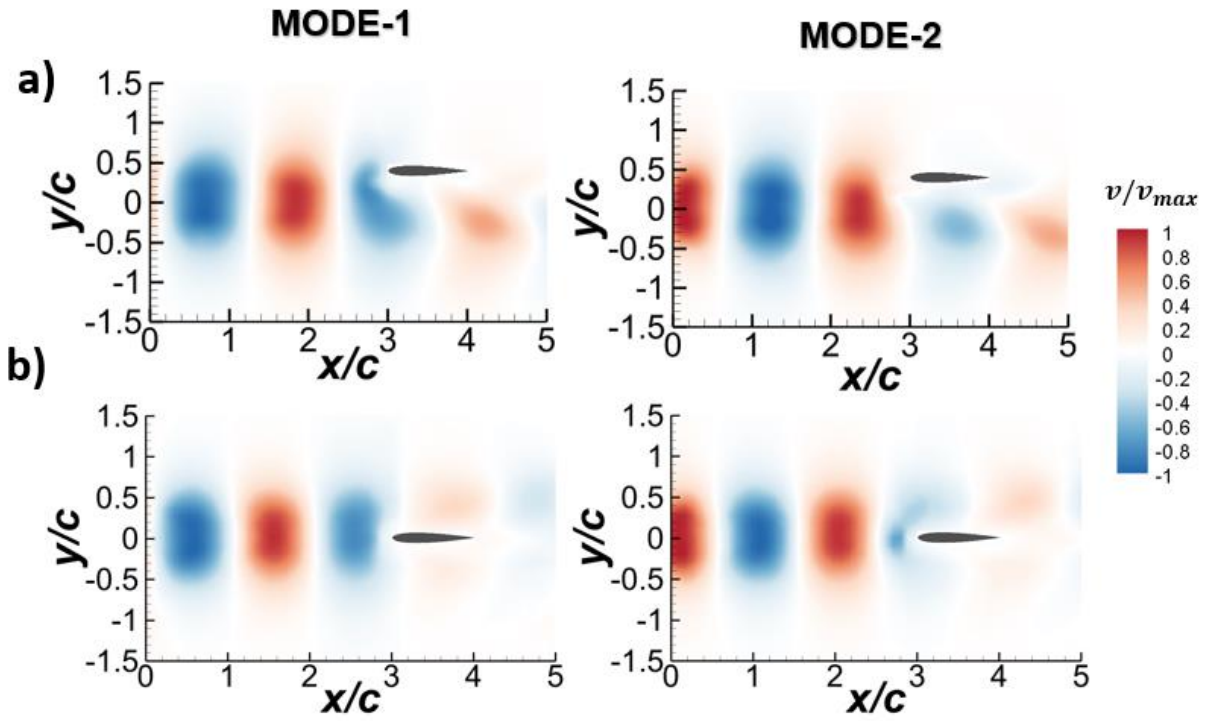

Figure 9 The first two POD modes of cross-stream velocity component for a) $y_{LE}/c = 0.4$ (with fraction of total energy of 26.6% and 24.6%); b) $y_{LE}/c = 0$ (with fraction of total energy of 26.4% and 23.8%); for *A*/*c*=0.4, *k*=1.70, *St*=0.22.

C. Loaded wing in the wake

In this section we focus on the cases when the wing is set at a nonzero angle of attack α_{wing}. The wake parameters were kept the same as *A*/*c* = 0.4, *k* = 1.70, while the upstream plunging airfoil is also set at the mean angle of attack of $\alpha_{airfoil}$ = 0° to produce symmetrically generated wakes. For three offset locations, $y_{LE}/c = -0.2,$ 0, and 0.2, we present the variations of the phase-averaged lift coefficient and the vorticity fields at *t*/*T* = 0.5 in Figure 11 for $\alpha_{wing} = 5°$ and in Figure 12 for $\alpha_{wing} = 10°$. The most obvious difference in the flow fields with nonzero angle of

attack is the increased evidence of flow separation and formation of the leading-edge vortices. This becomes more pronounced with increasing angle of attack and for $y_{LE}/c \leq 0$ as the counter-clockwise vortices induce separation at the leading-edge. The incoming counter-clockwise vortices

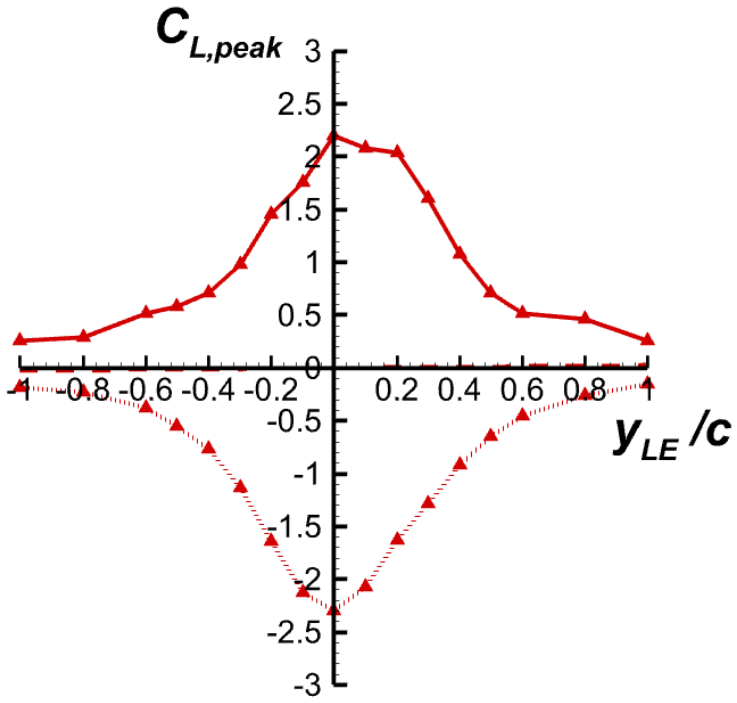

Figure 10 Maximum and minimum phase-averaged lift coefficient as a function of offset distance of the wing y_{LE}/c for *A*/*c*=0.4, *k*=1.70, *St*=0.22.

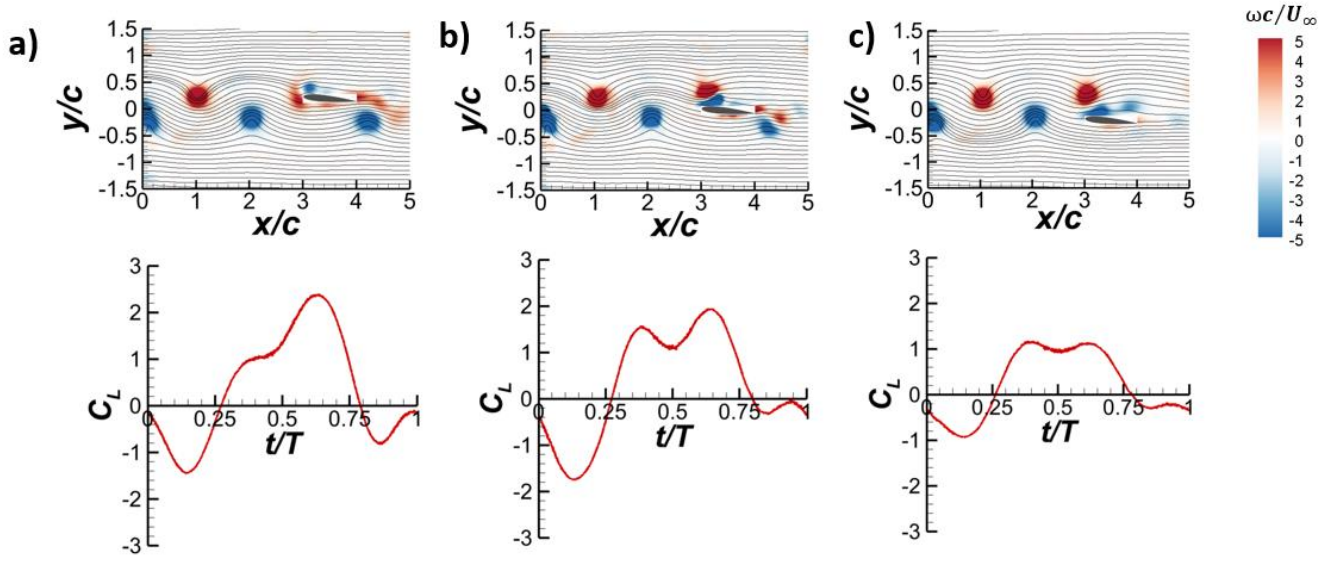

Figure 11 For $\alpha_{wing} = 5°$, vorticity contours with streamlines at phase *t*/*T*=0.5 (top), and time history of phase-averaged lift coefficient (bottom) for a) $y_{LE}/c = 0.2$, b) $y_{LE}/c = 0$, c) $y_{LE}/c = -0.2$, for *A*/*c*=0.4, *k*=1.70, *St*=0.22.

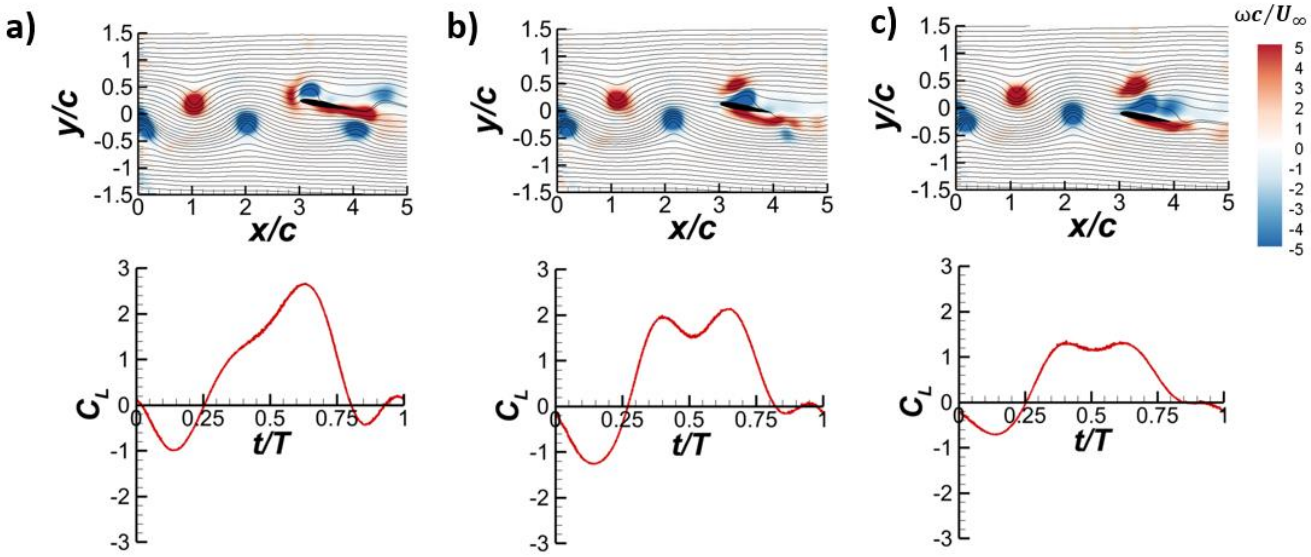

Figure 12 For $\alpha_{wing} = 10°$, vorticity contours with streamlines at phase *t*/*T*=0.5 (top), and time history of phase-averaged lift coefficient (bottom) for a) $y_{LE}/c = 0.2$, b) $y_{LE}/c = 0$, c) $y_{LE}/c = -0.2$, for *A*/*c*=0.4, *k*=1.70, *St*=0.22.

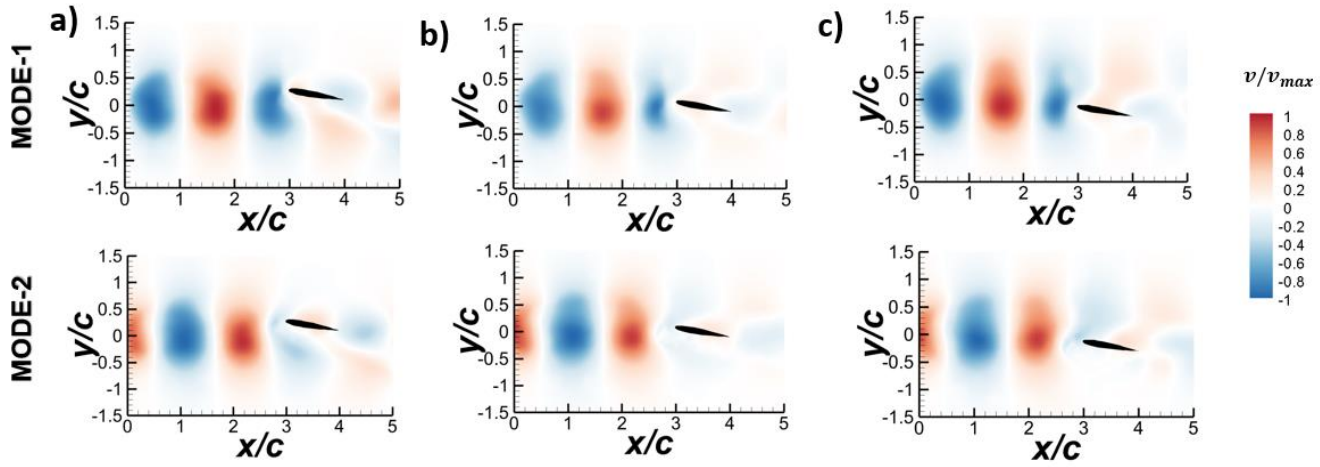

Figure 13 First two POD modes of cross-stream velocity component for $\alpha_{wing} = 10°$, a) $y_{LE}/c = 0.2$ (energy fraction of 25.1% and 23.1%), b) $y_{LE}/c = 0$ (energy fraction of 25.8% and 23.3%), c) $y_{LE}/c = -0.2$ (energy fraction of 23.7% and 21.9%) for *A*/*c*=0.4, *k*=1.70, *St*=0.22.

in the wake form vortex dipoles with the leading-edge vortices. However, for both angles of attack, the largest lift fluctuations occur for a positive offset value, y_{LE}/c = 0.2. This occurs soon after the counter-clockwise vortices directly impinge on the wing leading-edge and cause the formation

of the leading-edge vortex as seen at t/T = 0.5. The peak lift is observed a little after this phase as the leading-edge vortex is likely to grow, shed and convect downstream. Hence, large local cross-stream velocity just upstream of the leading-edge as well as the leading-edge vortex formation contribute to the large lift peak in this case.

Figure 13 presents the first two dominant POD modes of the cross-stream velocity component for $\alpha_{wing} = 10°$ and three different values of the offset distance $y_{LE}/c = -0.2,\ 0,$ and 0.2. The first two modes in each case account for roughly the same amount of total energy and contain significantly more energy than the remaining modes. In all cases, the energy level of the first two modes is around 48%, which is slightly less than that for $\alpha_{wing} = 0°$ (approximately 50%). We conclude that there is no significant influence of the offset distance and the angle of attack on the wake coherence in the measurement plane (spanwise plane).

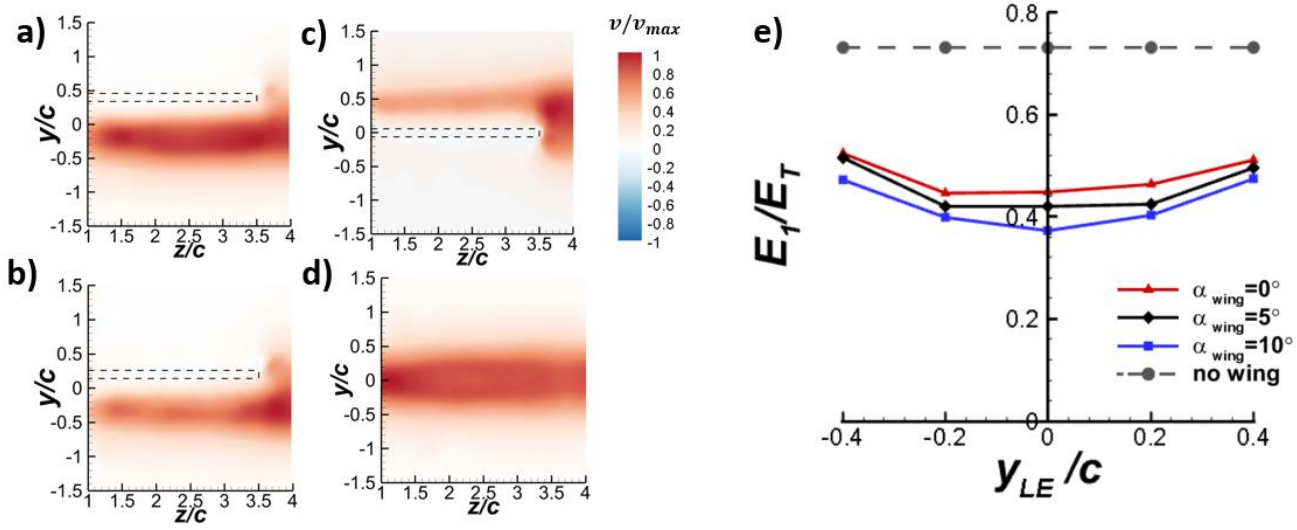

Figure 14 First POD mode of cross-stream velocity for $\alpha_{wing} = 0°$ and a) $y_{LE}/c = 0.4,$ b) $y_{LE}/c = 0.2,$ c) $y_{LE}/c = 0,$ d) in the absence of the wing; e) ratio of the energy of the first mode to the total energy for different angle of attack and offset locations at x/c=4.03; A/c=0.4, k=1.70, St=0.22.

The degree of two-dimensionality of the interaction can also be assessed in the cross-flow measurements at x/c = 4.03, which is immediately downstream of the trailing-edge. For three offset distances, Figure 14a-c present the first dominant modes of the cross-stream velocity fluctuations in the x/c = 4.03 plane. In these plots, the wing is illustrated with dashed lines. The POD modes

are roughly uniform in the spanwise direction, concentrated either above or below the wing depending on the offset distance. The uniformity of the first POD modes comes to an end near the

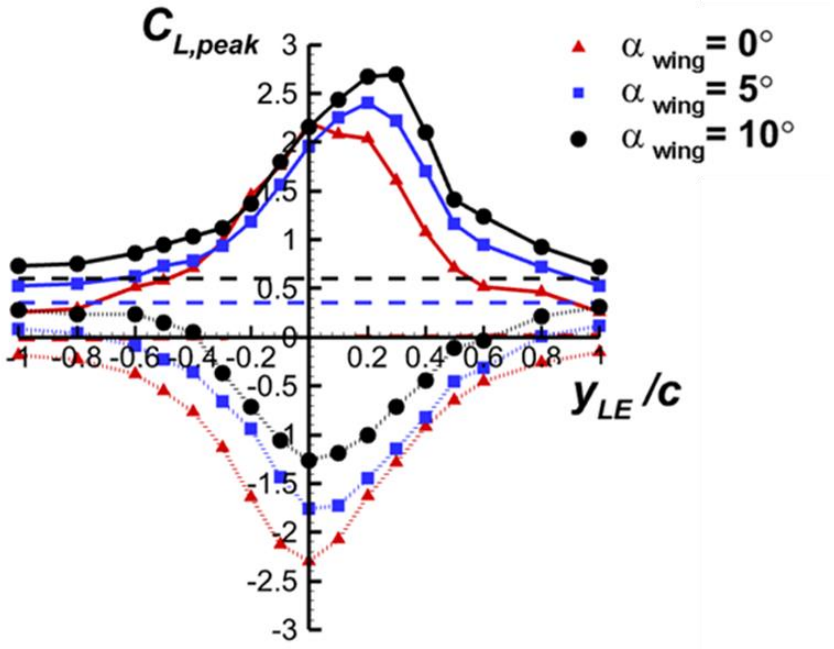

Figure 15 Maximum and minimum values of phase-averaged lift coefficient as a function of offset distance of the wing for A/c=0.4, k=1.70, St=0.22, $\alpha_{airfoil} = 0°$; the dashed lines show the corresponding lift coefficients in steady freestream.

wing-tip. Figure 14d shows the corresponding first POD mode of the cross-stream velocity fluctuations for the wake in the absence of the wing. The first mode, which can be described as a flapping mode for the cross-stream velocity fluctuations is dominant across a wide range of plunge frequency and amplitude (Turhan *et al*. [14]), while the higher modes have much smaller energy. For the wake parameters in Figure 14, the first dominant mode has more than 70% of the total energy. In the presence of the wing, the interaction with the wing causes significant drop in the energy of the first mode. However, the effect of wing angle of attack and the wing location (offset distance within the range tested) have much smaller effects.

Figure 15 shows the maximum and minimum phase-averaged lift coefficients as a function of offset distance for the wing angles of attack for $\alpha_{wing} = 0°$, 5°, and 10°. With increasing angle of attack, the magnitude of the positive peak lift coefficients generally increases whereas the magnitude of the negative lift coefficients decreases. The asymmetry with respect to the offset

distance increases with increasing angle of attack, shifting the largest positive peaks to positive offset distances (wing over the wake centerline). For $\alpha_{wing} = 10°$, the largest positive lift coefficient is found at $y_{LE}/c = 0.3$, whereas the lowest lift coefficient occurs when the wing is at the centre of the wake. The dashed lines show the corresponding lift coefficients in steady freestream. The effect of the vortex street appears to be limited to a region within approximately one chord length distance from either side of the centerline.

D. Wing in asymmetric wakes

The purpose of this section is to explore the effect of asymmetric wakes on the unsteady loading on the wing. The asymmetric wakes were produced by oscillating the upstream airfoil at nonzero angles of attack, $\alpha_{airfoil} = 5°$ and $10°$. We focussed on the unloaded wing case, i.e. $\alpha_{wing} = 0°$. The wake kinematic parameters were kept the same at $A/c = 0.4$, $k = 1.70$, and $St = 0.22$.

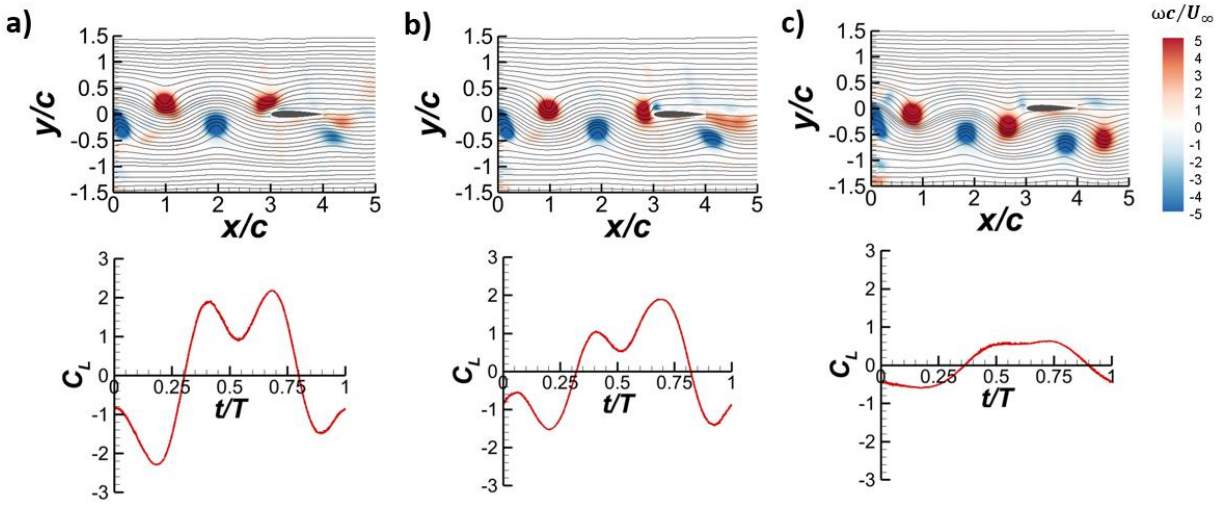

Figure 16 Vorticity contours with streamlines at t/T=0.5 (top row), and time history of phase-averaged lift coefficient over one cycle (bottom row) for a) $\alpha_{airfoil} = 0°$, b) $\alpha_{airfoil} = 5°$, c) $\alpha_{airfoil} = 10°$; $y_{LE}/c = 0$, A/c=0.4, k=1.70, St=0.22.

Figure 16 compares the phase-averaged vorticity fields at t/T = 0.5 (top row) and phase-averaged lift coefficient over one cycle (bottom row) for $\alpha_{airfoil} = 0°$, 5°, and 10°. For all three cases, the wing is located at the same cross-stream location of $y_{LE}/c = 0$. As expected, for

nonzero angles of attack of the airfoil, the wake of the oscillating airfoil is deflected downwards. There is no noticeable effect on the strength of the vortices, however this will be quantified as a next step in this article. With increasing angle of attack and a more deflected trajectory of the wake, the vortex street induces lower lift coefficients. For $\alpha_{airfoil} = 5°$, there is slight reduction in the

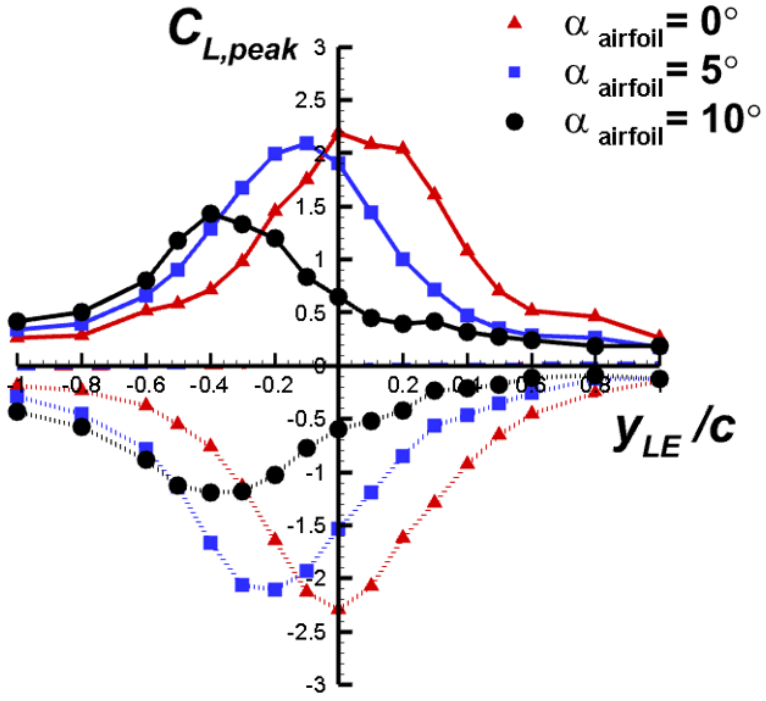

Figure 17 Maximum and minimum values of phase-averaged lift coefficient as a function of offset distance of the wing for $\alpha_{airfoil} = 0°, 5°,$ and 10°; for A/c=0.4, k=1.70, St=0.22, $\alpha_{wing} = 0°$.

positive peak lift coefficient even though the counter-clockwise rotating vortices directly impinge on the wing. The decrease in the magnitude of the peak negative lift coefficient is more noticeable as the counter-clockwise vortices are further away from the wing. For $\alpha_{airfoil} = 10°$, both positive and negative peak lift coefficients decrease significantly in magnitude. To characterize the effect of the offset distance of the wing, the wing was traversed in the asymmetric wakes.

Figure 17 shows the maximum and minimum lift coefficients as a function of the offset distance of the wing for $\alpha_{airfoil} = 0°, 5°,$ and 10°. As the wake becomes more deflected downwards with increasing angle of attack, the wing interacts directly with the vortex street at negative y_{LE} locations (below the airfoil), resulting in the location of the largest peak lift

coefficients shifting to more negative y_{LE} locations. We also observe that the magnitude of the largest peak coefficients decreases with increasing deflection of the vortex street. For the asymmetric wake of $\alpha_{airfoil} = 10°$, it is seen that the largest lift coefficient magnitude of the wing is approximately 30% lower than in the symmetric wake case. The maximum and minimum lift coefficients are found when the wing is placed at $y_{LE}/c = -0.4$.

For each of the three curves in Figure 17, we investigated the flow fields of the cases for which the largest lift fluctuations are observed. Figure 18 presents the vorticity fields (left column) and cross-stream velocity (middle column) at $t/T = 0.5$, and the time history of the phase-averaged lift coefficient (right column) for the cases of $\alpha_{airfoil} = 0°$, 5°, and 10°. The normalized circulation for approaching vortices is also added to the vorticity fields. The circulation was calculated by the method described in Cleaver *et al*. [36]. The center of the vortex is found by the location of the maximum vorticity and then a square path line around the vortex is defined. The circulation is calculated as the size of the square is increased until the changes are very small. For the symmetric wake $\alpha_{airfoil} = 0°$ and the slightly asymmetric case $\alpha_{airfoil} = 5°$, the strength of the clockwise and counter-clockwise vortices are similar. The corresponding contours of the cross-stream velocity component and the phase-averaged lift coefficients are also similar. For the largest deflection case ($\alpha_{airfoil} = 10°$), there is not much change in the circulation of the counter-clockwise vortex ($\Gamma/U_\infty c = 1.58$), however there is some reduction in the strength of the clockwise vortex ($\Gamma/U_\infty c = -1.30$) compared to the other cases. This is expected as the maximum and minimum effective angles of attack become more different in this case. There is also significant change in the topology of the vortex street. Whereas the wavelength appears to remain the same, the lower row of the vortices is shifted (no longer anti-symmetric) as the clockwise and counter-clockwise vortices are formed closer to each other. The vortex couples of opposite signs have an induced velocity with a downward component. (Similar change in the topology of the reversed Karman vortex street in the deflected wakes is seen for an oscillating NACA0012 airfoil at the nonzero mean angles of attack [26,36]. This change in the vortex street configuration modifies the approaching cross-stream velocity component significantly. There is slight reduction in the positive cross-stream velocity magnitude while the negative cross-stream velocity region becomes smaller. The changes in the cross-stream velocity together with decreased strength for the clockwise vortices result in smaller lift fluctuations for the deflected vortex streets.

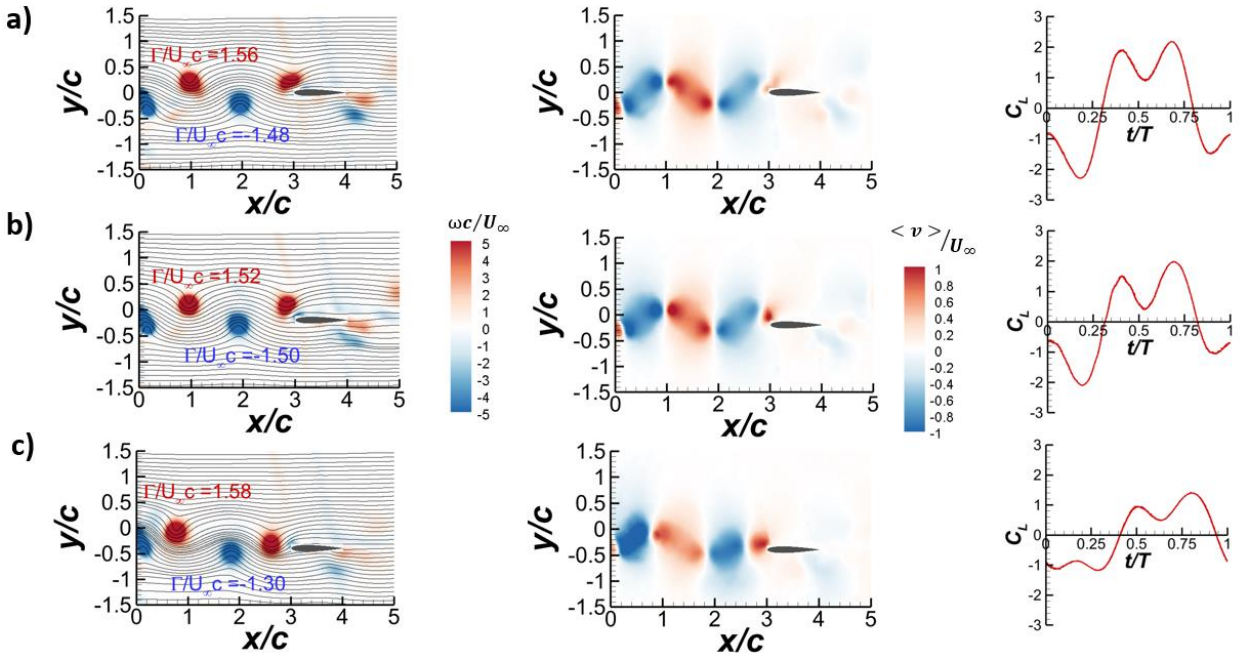

Figure 18 Contour plots of vorticity with streamlines (left column) at *t/T*=0.5; cross-stream velocity (middle column) at *t/T*=0.5; time history of phase-averaged lift coefficient over one cycle for a) $\alpha_{airfoil} = 0°,\ y_{LE}/c = 0$, b) $\alpha_{airfoil} = 5°, y_{LE}/c = -0.2$, c) $\alpha_{airfoil} = 10°,\ y_{LE}/c = -0.4$. The kinematic parameters are *A/c*=0.4, *k*=1.70, *St*=0.22, and $\alpha_{wing} = 0°$.

E. Effects of plunge frequency and amplitude on wake-wing interaction

In this section, we investigate the effects of the reduced frequency *k* and oscillation amplitude *A/c* on the characteristics of the travelling gusts generated, vortex street – wing interaction, and the resulting lift coefficient fluctuations. We focus on the unloaded wing ($\alpha_{wing} = 0°$) in the symmetrically generated wakes ($\alpha_{airfoil} = 0°$) and the head-on collision cases ($y_{LE}/c = 0$).

Figure 19a to 19d present the first two POD modes of the cross-stream velocity component for *A/c* = 0.2 and varying reduced frequency *k* = 0.63, 1.26, 1.88, and 2.51. These fundamental wake modes have decreasing wavelength and cross-stream length scale with increasing reduced frequency *k*. While the first and second modes have approximately the same energy percentages, the sum of the energy of the two modes increases as a fraction of the total energy with increasing reduced frequency. The ratio of the energy of the wake modes to the total energy increases from 5.5% for *k* = 0.63, 22.8% for *k* = 1.26, 38.1% for *k* = 1.88 to 49.2% for *k* = 2.51 at an amplitude of *A/c* = 0.2. The wake modes upstream of the wing appear undisturbed until the immediate

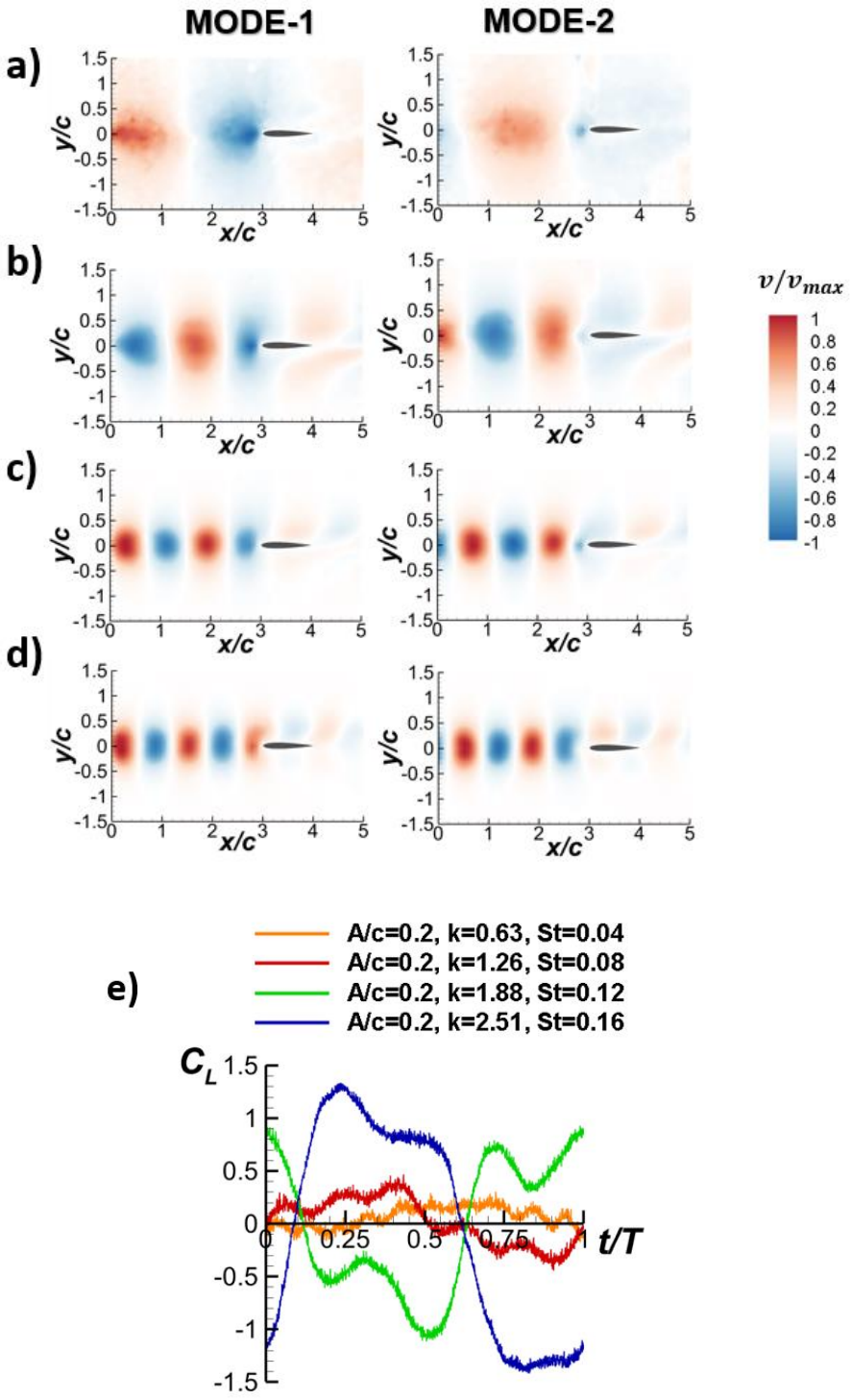

Figure 19 First two POD modes of cross-stream velocity component for a) k = 0.63, St = 0.04 (with fraction of total energy of 3.3% and 2.2%); b) k= 1.26, St = 0.08 (with fraction of total energy of 11.8% and 11.0%); c) k= 1.88, St = 0.12 (with fraction of total energy of 20.2% and 17.9%); d) k= 2.51, St = 0.16 (with fraction of total energy of 26.4% and 22.8%); and e) time history of phase-averaged lift coefficient over one cycle; for A/c=0.2, α_{wing} =0°, $\alpha_{airfoil} = 0°$, and $y_{LE}/c = 0$.

neighbourhood of the leading-edge of the wing, but then disintegrate quickly over the wing and downstream.

Figure 19e reveals that the peak lift coefficients increase with increasing reduced frequency at constant plunge amplitude. The timing of the peaks varies with the reduced frequency since the wavelength and the arrival time to the leading-edge of the wing are dependent on the reduced frequency as expected from the POD modes. This figure shows that the wavelength of the vortex streets varies. The distance from the origin of the wake (trailing-edge of the plunging airfoil) to the leading-edge of the wing is fixed. Also, the convection speed is roughly constant (see the discussion of Figure 6(a)). Hence, the arrival time of the vortices near the leading-edge is nearly constant. However, constant arrival time corresponds to varying phase (time normalized by the period). In addition, the waveforms for the phase-averaged lift coefficient exhibit many higher harmonics for the lower reduced frequencies. For the lowest reduced frequency of $k = 0.63$, we found the Fourier coefficients (not shown here) of the phase-lift coefficient at odd terms, $n = 3, 5, 7, 9$. For $k = 1.26$, the 3rd and 5th modes are most significant. For higher reduced frequencies, $k = 1.88$ and 2.51, the most significant Fourier mode is $n = 3$ and it can reach as high as 50% of the coefficient of $n = 1$.

We recall that the cross-stream velocity along the centerline in the undisturbed wake is primarily predicted to depend on the vortex array aspect ratio b/λ according to Equation (8). In turn, Figure 6b shows that the experimentally measured ratio b/λ is a strong function of the reduced frequency k and the normalized amplitude of the plunging motion A/c. For $A/c = 0.2$, the aspect ratio of the vortex street increases almost linearly (we could not get a reliable estimate of b based on the two-point cross-correlations of the spanwise vorticity for the lowest reduced frequency as the two rows are very close to each other). In Figure 20a, we plot the cross-stream velocity component over a wavelength for various reduced frequencies using Equation (8). At the lower frequency ($k = 1.26$), the predicted cross-stream velocity component has multiple peaks, whereas at the highest reduced frequency of $k = 2.51$, the waveform becomes more similar to a sine-wave. We calculated the Fourier coefficients (not shown here) of the predicted cross-velocity profiles. We found that, at $k = 1.26$, the Fourier coefficients are significant at $n = 3$ and 5, whereas at higher reduced frequencies only $n = 3$ becomes dominant. In summary, the predicted waveforms of the cross-stream velocity in the vortex street could explain the higher harmonics observed in the measured phase-averaged lift coefficient.

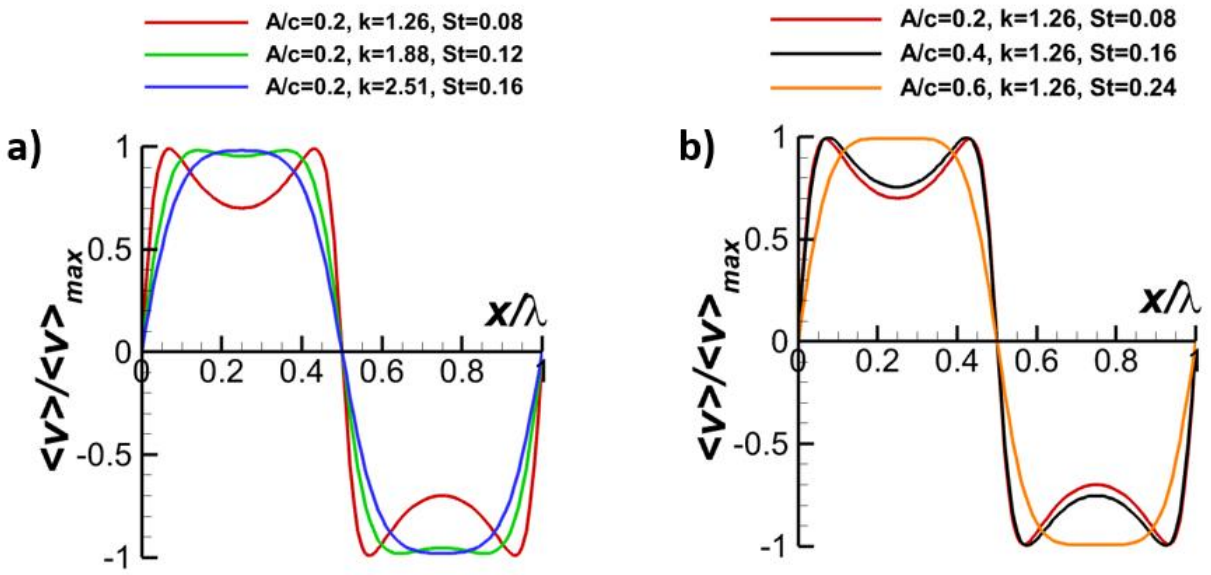

Figure 20 Cross-stream velocity component according to the point vortex model for a) A/c = 0.2 and varying k; b) k = 1.26 and varying A/c.

Next, we present the effects of varying amplitude A/c = 0.05; 0.1; 0.2; 0.4; 0.6 at fixed reduced frequency k = 1.26. Figure 21a to 21e presents the first two dominant POD modes of the cross-stream velocity component for the corresponding cases. Again, the relative energy of the first two modes, which characterize the travelling fundamental wake modes, increases as the amplitude A/c increases. Also, the cross-stream extent of the POD modes increases with increasing amplitude A/c, while the wavelength remains constant. For the largest amplitude of A/c = 0.6, double peaks develop away from the centerline (nevertheless the amplitude is roughly constant in this region). For all other cases, the local maximum is at the wake centerline. Figure 21f shows the variation of the phase-averaged lift coefficient for the corresponding cases. The magnitudes of the maximum and minimum lift coefficients increase with increasing amplitude A/c. As the wavelength remains the same for all cases, the waveforms are overall similar. However, small amplitude cases exhibit higher harmonics. The Fourier coefficients were calculated (not shown here) and it was found that n = 5 has the largest amplitude for A/c = 0.05, while for A/c = 0.1; 0.2 and 0.4, the modes n = 3 and 5 have comparable amplitudes.

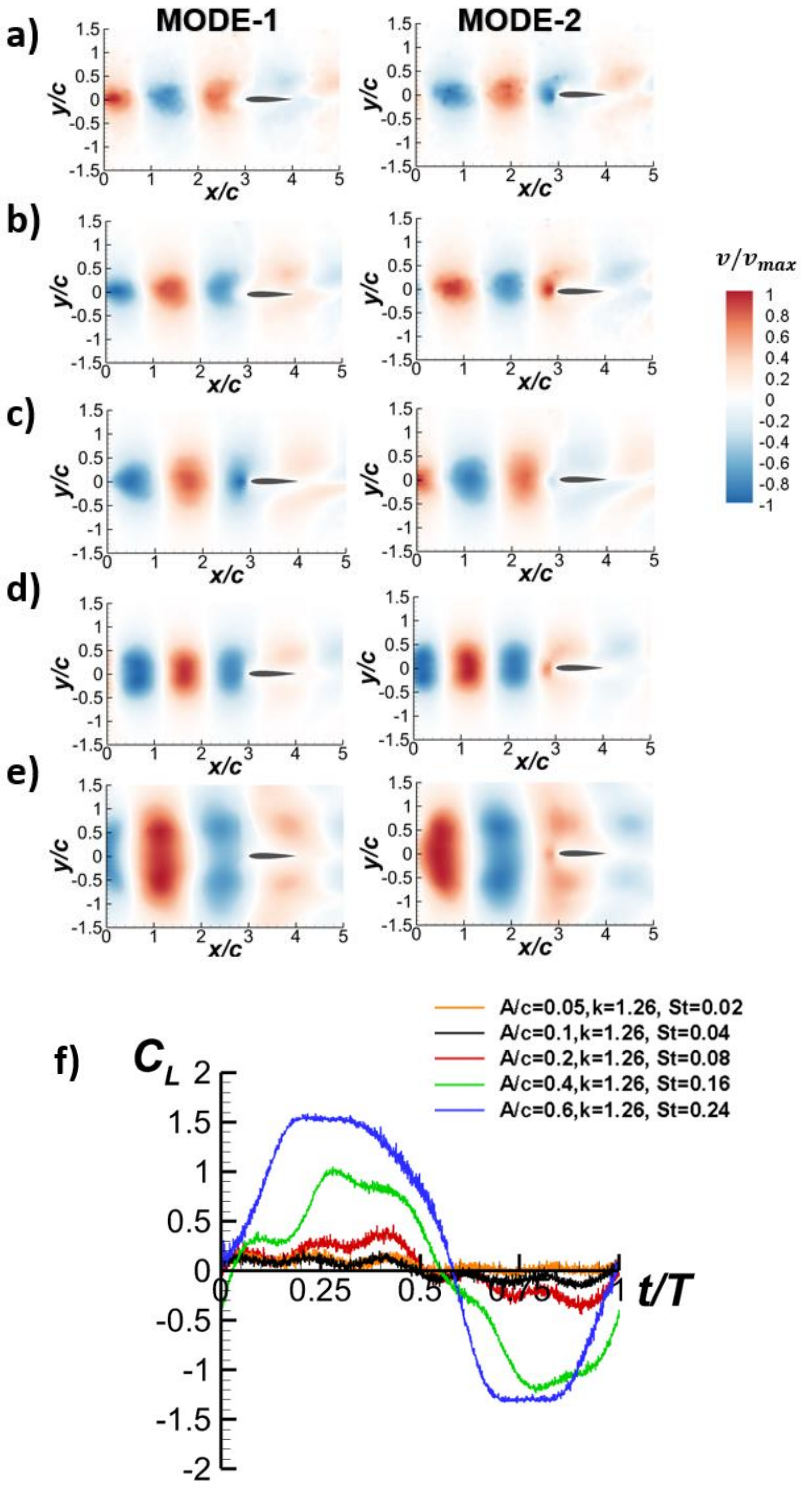

Figure 21 First two POD modes of cross-stream velocity component for a) *A/c* = 0.05, *St* = 0.02 (with fraction of total energy of 3.5% and 3.2%); b) *A/c* = 0.1, *St* = 0.04 (with fraction of total energy of 3.7% and 3.6%); c) *A/c* = 0.2, *St* = 0.08 (with fraction of total energy of 11.8% and 11.0%); d) *A/c* = 0.4, *St* = 0.16 (with fraction of total energy of 27.6% and 24.6%); e) *A/c*=0.6, *St*=0.24 (with fraction of total energy of 30.6% and 29.9%); and f) time history of phase-averaged lift coefficient over one cycle; for k = 1.26, α_{wing} =0°, $\alpha_{airfoil} = 0°$, and $y_{LE}/c = 0$.

Again, using the point vortex model of the vortex street (Equation (8)) and the measured values of b/λ presented in Figure 6b, we can explain the trends of higher harmonics. For the smallest amplitudes, again, we could not measure accurately the distance b as the two rows are very close to each other. For the remaining three amplitudes, Figure 20b shows the variations of the cross-stream velocity over a wavelength. The existence of the higher harmonics can be expected based on these waveforms. For the two smallest frequencies in Figure 20b, we find that n =3 and 5 are dominant in Fourier coefficients, although n = 3 has larger amplitude. For the largest amplitude case, we expect to find smaller number of harmonics (only n = 3 dominant). These predictions are consistent with the observed waveforms of the phase-averaged lift coefficients in Figure 21f.

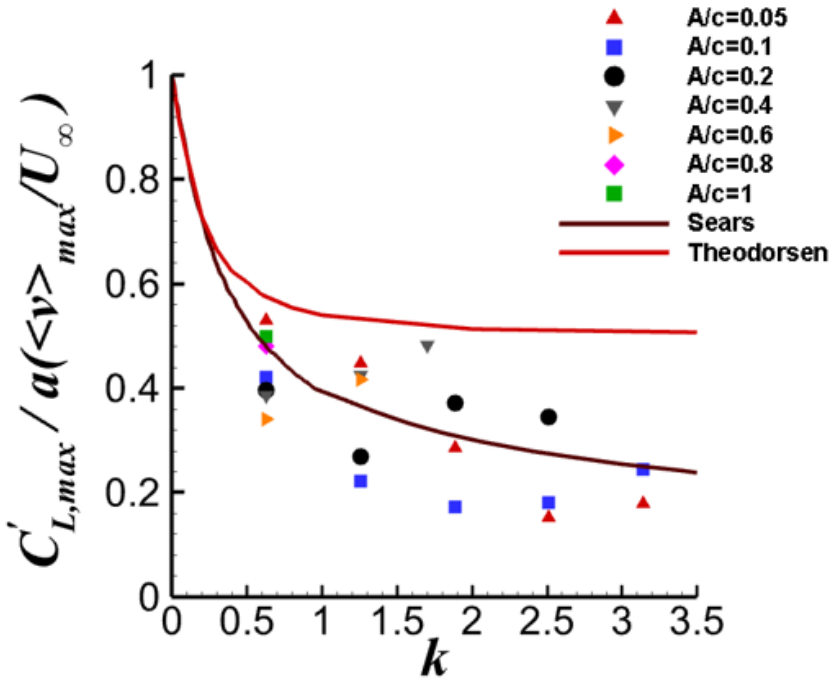

Figure 22 Normalized amplitude of the fluctuations of the lift coefficient as a function of reduced frequency for $\alpha_{wing} = 0°$, $\alpha_{airfoil} = 0°$.

We summarized the results for varying amplitude A/c and reduced frequency k in Figure 22. Here the amplitude of the lift coefficient was normalized using the static lift coefficient slope a of the wing and the ratio of the maximum phase-averaged cross-stream velocity divided by the freestream velocity. The ratio of the maximum cross-stream velocity divided by the freestream velocity can be interpreted as the maximum effective angle of attack since the mean angle of attack

is zero in this case. Surprisingly, for plunging airfoils, the ratio of the maximum lift coefficient to the maximum effective angle of attack is always close to 2π or slightly below [24], even though the velocity fluctuations are not small. Given that in our case the variation of the static lift coefficient as a function of angle of attack is highly nonlinear (see Figure 4a), we used a constant value of the slope a calculated by using 2π for the airfoil cross-section and the Prandtl's lifting line theory, assuming an elliptical circulation variation. Figure 22 reveals that, despite the fact that velocity fluctuations are not small, the trend is similar to that of the Sears theory [38] and the magnitude is smaller than that of the Theodorsen theory [39]. This may be somewhat expected as the unsteady wake of the plunging airfoil produces a travelling wave, which resembles a Sears gust. Nevertheless, there is still large scatter in the data for a fixed value of the amplitude *A/c* as well as a large scatter from the Sears theory.

The scatter of the data from the Sears theory may be due to not only the large amplitude velocity fluctuations, but also due to the unsteady wake being not exactly like the gusts modelled by the Sears theory. To examine the latter possibility, we calculated the two-point cross-correlation of the cross-stream velocity component C_{vv} as defined in Equation (5) for an arbitrary location and taking a fixed reference point. The cross-stream velocity of the gusts modelled by the Sears theory can be expressed as:

$$v' = V_{amp}\cos\left(2\pi\frac{x}{\lambda} - 2\pi f t\right) \tag{9}$$

where V_{amp} is a constant, which implies that the gust amplitude is uniform in the cross-stream direction. By taking the fixed reference point at (x = 0, y = 0), the two-point cross-correlation of the cross-stream velocity fluctuations can be calculated for the uniform (Sears) gust as:

$$C_{vv,Sears} = \cos\left(2\pi\frac{x}{\lambda}\right) \tag{10}$$

Figure 23a shows the variation of the two-point cross-correlation coefficient in the absence of the wing as a function of the x-axis normalized by the wavelength for a fixed reduced frequency of k = 1.26 and various amplitudes *A/c*. The calculated cross-correlation coefficients are compared with that of the uniform (Sears) gust. With increasing amplitude *A/c*, there is a trend of the cross-correlation coefficient approaching that of the uniform (Sears) gust. However, at low amplitudes, the cross-correlation coefficient decays rapidly in the streamwise direction. In addition to the changes in the shape and decay rate of the variation, higher harmonics are also visible. At low amplitudes, the cross-correlation coefficient is far away from that of a uniform gust.

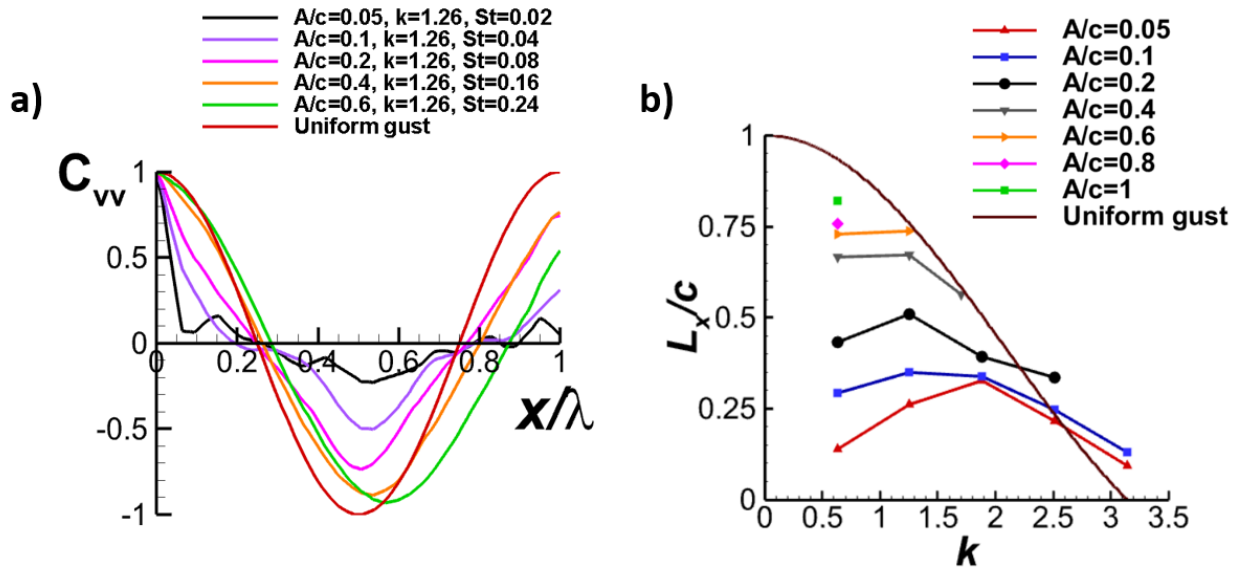

Figure 23 Variation of a) cross-correlation coefficient in the absence of the wing as a function of x/λ (reference location is at (x/c=3.5, y=0); b) integral length scale as a function of reduced frequency k.

Using the cross-correlation coefficient in the streamwise direction, one can define the streamwise length-scale as:

$$L_x = \int_0^c \mathrm{C_{vv}}(x,\, y=0)\mathrm{d}(x) \tag{11}$$

The streamwise integral length scale L_x for the uniform (Sears) gust is found as:

$$\frac{L_x}{c} = \frac{\sin(k)}{k} \tag{12}$$

The integral length scale for all cases is shown in Figure 23b as a function of reduced frequency k and compared with that of the uniform gust. This parameter reflects the effects of the streamwise decay as well as the departure from the fundamental harmonic waveform. At low reduced frequencies and low amplitudes A/c, the deviation from the uniform gust is large. As the streamwise integral scale approaches that of the Sears gust with increasing reduced frequency and amplitude A/c, there is a suggestion that the Strouhal number based on the amplitude might be the dominant parameter.

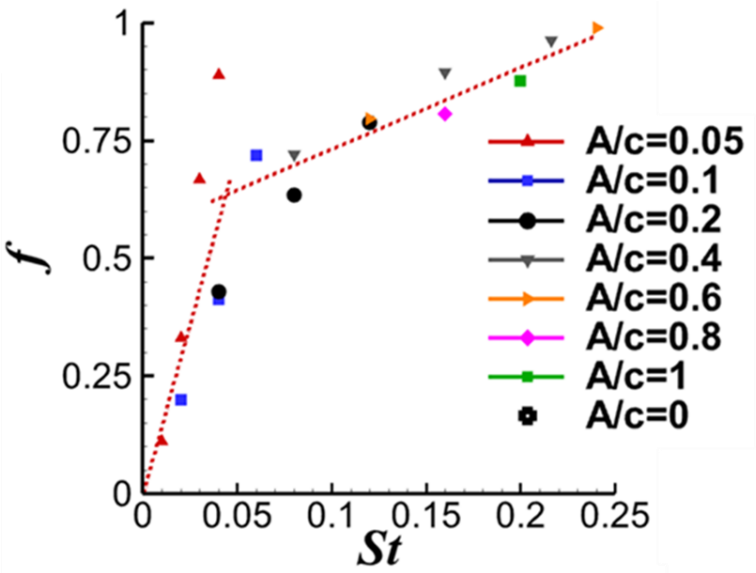

Figure 24 Variation of gust shape factor as a function of Strouhal number *St* in the absence of the wing.

The degree of departure from the Sears gust can be quantified by defining the *shape factor* as:

$$f = \frac{(L_x/c)_{measured}}{(L_x/c)_{uniform\ gust}} \tag{13}$$

The variation of the shape factor *f* is shown as a function of the Strouhal number in Figure 24. In general, the shape factor increases with increasing Strouhal number. Hence the streamwise integral scale approaches that of the Sears gust. Two different regions of the Strouhal number can be identified in Figure 24. For low Strouhal numbers $St \leq 0.05$ approximately, the shape factor increases very rapidly. For $St > 0.05$, the shape factor increases more slowly. Interestingly, for the unsteady wake of the plunging airfoil at the same Reynolds number (Re = 20,000), we reported that $St = 0.05$ is the approximate border between the drag and thrust (net streamwise force produced by the plunging airfoil is zero) [14]. In summary, how close the unsteady wake is to the gusts modelled by the Sears theory depends mainly on the Strouhal number. At low Strouhal numbers (wake mode), the wake is not very similar to the Sears gust, whereas at high Strouhal numbers (thrust mode) the wake becomes more similar to the Sears gust.

Turhan *et al*. [14] also showed that the coherence of the unsteady near wake increases with Strouhal number. The first two POD modes have increasingly larger fraction of the total energy

with increasing *St*. In addition, the spanwise-averaged cross-correlation of the cross-stream velocity increases rapidly up to *St* ≈0.05, and then remains constant at a value of approximately 0.92 for larger Strouhal numbers. In summary, with increasing Strouhal number, the wake becomes more similar to the Sears gust while the coherence of the streamwise flow and crossflow increases.

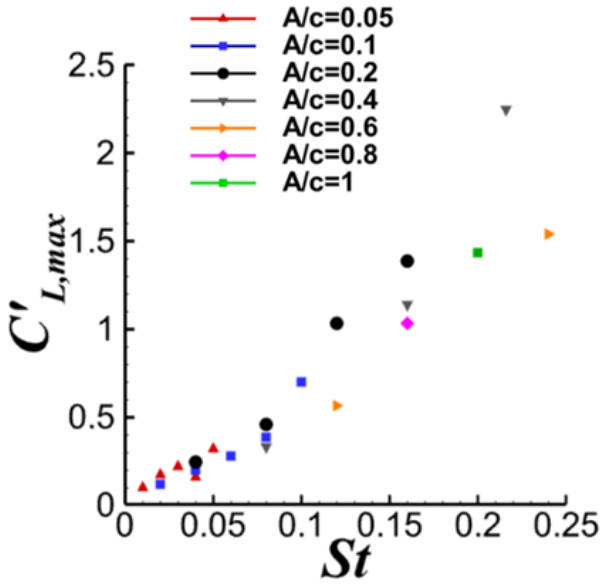

Figure 25 Amplitude of the lift coefficients as a function of Strouhal number *St* for all cases, $\alpha_{wing} = 0°$, $\alpha_{airfoil} = 0°$.

Finally, we plot the variation of the amplitude of the lift coefficient as a function of Strouhal number in Figure 25. This figure could be compared with Figure 22, in which the normalized lift coefficient is plotted as a function of the reduced frequency. There is a better collapse of the data with the Strouhal number compared to the reduced frequency. This stems from two facts. Firstly, we have shown that the unsteady features of the wake, including the amplitude of the cross-stream velocity fluctuations, coherence, or degree of two-dimensionality of the streamwise flow and crossflow, and the waveforms of the gust velocity profiles, all are strong functions of the Strouhal number. Secondly and more importantly, the Strouhal number itself is the ratio of the maximum plunging velocity to the freestream velocity, hence an amplitude parameter for the wakes/gusts. As a result, a single parameter, which is the Strouhal number based on the amplitude of the wake-producing airfoil, determines the maximum lift coefficient. This is contrasted with the Sears theory for small-amplitude disturbances in which the reduced frequency is the primary parameter.

IV. CONCLUSIONS

The unsteady aerodynamics of a finite wing submerged in the wake of a periodically plunging upstream airfoil was investigated in water tunnel experiments at a Reynolds number of Re = 20,000. Interaction of the vortex street configurations with varying wavelength and circulation with the stationary downstream wing was studied by means of velocity measurements and unsteady lift force measurements. The unsteady wakes of the oscillating airfoil produce travelling gusts with finite cross-stream extent, while very large velocity fluctuations exceeding the freestream velocity are possible within the wake. The properties of the unsteady wakes, including the wavelength of the vortex street, the spacing between the vortex rows in the cross-stream direction, and the maximum rms velocity of the cross-stream velocity, were characterized. The streamwise flow can be represented with the first two POD modes, which are the fundamental wake modes. On the other hand, a single mode which is a flapping mode represents the cross-stream velocity field in a crossflow plane. The relative energy of the POD modes and the magnitudes of the two-point cross-correlations increase with increasing Strouhal number based on the amplitude of the upstream oscillating airfoil, implying that the coherence (degree of the two-dimensionality) increases.

We focussed on the kinematic parameters of the wake (amplitude and frequency) that produce the largest cross-stream velocity amplitude within our range of parameters. Then we investigated the interaction of the wake for the unloaded wing (set at zero angle of attack) and the loaded wings as well as for the wing in asymmetric wakes (generated by oscillating the upstream airfoil at nonzero mean angle of attack). For the unloaded wing, the largest amplitude of the lift fluctuations occurs for the direct head-on interaction when the leading-edge of the wing is located at the wake centerline. This is consistent with the fact that the two dominant POD modes of the cross-stream velocity have a maximum at the wake centerline. Even for this case, the flow separation at the leading-edge does not appear significant. Yet, the reversed Karman vortex street configuration loses its coherence after the interaction with the wing. When the wing is located further away from the wake centerline, the lift time history has a single dominant frequency, which is the fundamental wake frequency and also the plunging frequency of the airfoil. In contrast, as the wing approaches the wake centerline, higher harmonics in the lift history become significant. When the wing is located at the wake centerline, the most significant harmonic in the lift is n = 3 for these wake parameters, although one may intuitively expect n = 2 for the staggered reversed

Karman vortex street arrangement. As the PIV measurements are not time-accurate, we looked at the variation of the cross-stream velocity along the centerline (x, $y = 0$) in the approaching wake and upstream of the wing. The variation of the cross-stream velocity along the centerline also confirms that the most significant harmonic is $n = 3$. The measured cross-stream velocity is similar to the point vortex model of the undisturbed reversed Karman vortex street.

For the loaded wing, and with increasing angle of attack of the wing, the flow separation at the leading-edge, formation of a leading-edge vortex and formation of a vortex couple with the incident vortex become more noticeable. These observations strongly depend on the offset distance between the wing leading-edge and wake centerline. However, the formation of stronger leading-edge vortices does not necessarily correlate with larger amplitude of the lift oscillations. The largest amplitude of the lift coefficient occurs when the wing is located above the wake centerline and directly interacting with the counter-clockwise vortices of the reversed Karman street. For the inclined asymmetric wakes generated by plunging the airfoil at nonzero angle of attack, the location of the largest amplitude of the lift fluctuations shifts below the streamwise axis as the wake is deflected downwards. The magnitude of the largest peak lift coefficients decreases with increasing deflection angle of the wake (increasing angle of attack of the plunging airfoil). This is due to the unequal strength of the clockwise and counter-clockwise vortices as well as the changes in the topology of the staggered vortex street as the upper and lower rows are shifted with respect to each other.

For the general case of the unloaded wing in the symmetric (undeflected) wakes, the peak lift coefficients increase with increasing frequency and amplitude A/c of the plunging airfoil. At low frequencies and amplitudes, the waveforms of the phase-averaged lift coefficient reveal higher harmonics (up to $n = 5$), which again can be predicted by the point vortex model of the reversed Karman street. The amplitude of the lift coefficient normalized by using the maximum phase-averaged cross-stream velocity magnitude has a similar trend to the Sears function when plotted as a function of the reduced frequency, but with large scatter. It was shown that the cross-stream velocity not only has large amplitude and finite cross-stream extent, but also significant departure from a harmonic gust at low frequencies and amplitudes A/c. The properties of the gust waveform and the degree of the two-dimensionality are strong functions of the Strouhal number of the wake only. In addition, the Strouhal number is the ratio of the maximum plunge velocity of the plunging airfoil to the freestream velocity, hence an amplitude parameter for the unsteady wake. As a result,

the amplitude of the lift coefficient of the stationary wing is a strong function of the Strouhal number of the wake only.

ACKNOWLEDGMENTS

The authors would like to acknowledge the Engineering and Physical Sciences Research Council (EPSRC) strategic equipment Grant (EP/K040391/1) that made the velocity measurements possible and the Republic of Turkey Ministry of National Education Scholarship for the first author. For the purpose of open access, the authors have applied a Creative Commons Attribution (CC-BY) licence to any Author Accepted Manuscript version arising.

Data Availability: The data that support the findings of this study are available from the corresponding author upon reasonable request.

REFERENCES

[1] D. Rockwell, Vortex-body interactions, Annu. Rev. Fluid Mech. **30**, 199 (1998).

[2] I. Gursul, and D. Rockwell, Vortex street impinging upon an elliptical leading edge, Journal of Fluid Mechanics. **211**, 211 (1990).

[3] V. Durgesh, R. Padilla, E. N. Garcia, and H. Johari, *Impact of Coherent Structures on Aerodynamics Performance at Low Reynolds Numbers* (AIAA SciTech 2019 Forum, San Diego, CA, 2019). AIAA-2019-0847

[4] J. N. Lefebvre, and A. R. Jones, Experimental investigation of airfoil performance in the wake of a circular cylinder, AIAA Journal **57**, 2808 (2019).

[5] Z. Zhang, Z. Wang, and I. Gursul, Lift enhancement of a stationary wing in a wake, AIAA Journal **58**, 4613 (2020).

[6] J. J. Allena, and J. Smits, Energy harvesting eel, Journal of Fluids and Structures **15**, 629 (2001).

[7] K. Streitlien, G. S. Triantafyllou, and M. S. Triantafyllou, Efficient foil propulsion through vortex control, AIAA Journal **34**, 2315 (1996).

[8] P. B. Lissaman, and C. A. Shollenberger, Formation flight of birds, Science **168**, 1003 (1970).

[9] D. E. Alexander, Unusual Phase-Relationships between the Forewings and Hindwings in Flying Dragonflies, Journal of Experimental Biology **109**, 379 (1984).

[10] F. O. Lehmann, Wing–wake interaction reduces power consumption in insect tandem wings, Experiments in Fluids **46**, 765 (2009).

[11] B. M. Boschitsch, P. A. Dewey, and A. J. Smits, Propulsive performance of unsteady tandem hydrofoils in an in-line configuration, Physics of Fluids **26**, 051901 (2014).

[12] M. Ghommem, and V. M. Calo, Flapping wings in line formation flight: a computational analysis, The Aeronautical Journal **118**, 485 (2014).

[13] A. R. Jones, O. Cetiner, and M. J. Smith, Physics and Modeling of Large Flow Disturbances: Discrete Gust Encounters for Modern Air Vehicles, Annual Review of Fluid Mechanics **54**, 469 (2021).

[14] B. Turhan, Z. Wang, and I. Gursul, Coherence of unsteady wake of periodically plunging airfoil, Journal of Fluid Mechanics **938**, (2022).

[15] J. Gilman, and R. M. Bennett, Wind-tunnel technique for measuring frequency-response functions for gust load analyses, Journal Aircraft **3**, 535 (1966).

[16] E. R. Booth, and J. C. Yu, Two-dimensional blade-vortex flow visualization investigation, AIAA Journal **24**, 1468 (1986).

[17] M. C. Wilder, and D. P. Telionis, Parallel blade-vortex interaction, J. Fluids Struct. **12**, 801 (1998).

[18] V. Brion, A. Lepage, Y. Amosse, D. Soulevant, P. Senecat, J. C. Abart, and P. Paillart, Generation of vertical gusts in a transonic wind tunnel, Exp. in Fluids **56**, (2015).

[19] N. J. Wei, J. Kissing, and C. Tropea, Generation of periodic gusts with a pitching and plunging airfoil, Exp. in Fluids **60**, 1 (2019a).

[20] N. J. Wei, J. Kissing, T. T. B. Wester, S. Wegt, K. Schiffmann, S. Jakirlic, M. Holling, J. Peinke, and C. Tropea, Insights into the periodic gust response of airfoils, Journal of Fluid Mechanics **876**, 237 (2019b).

[21] Z. L. Wu, G. Bangga, T. Lutz, G. Kampers, and M. Holling, Insights into airfoil response to sinusoidal gusty inflow by oscillating vanes, Physics of Fluids **32**, 125107 (2020).

[22] W. P. Jones, and J. A. Moore, Flow in the wake of a cascade of oscillating airfoils, AIAA Journal **10**, 1600 (1972).

[23] J. Bicknell, and A. G. Parker, A wind-tunnel stream oscillation apparatus, Journal Aircraft **9**, 446 (1972).

[24] N. Chiereghin, D. J. Cleaver, and I. Gursul, Unsteady Lift and Moment of a Periodically Plunging Airfoil, AIAA Journal **57**, 208 (2019).

[25] S. F. Heathcote, Flexible flapping airfoil propulsion at low Reynolds numbers, PhD Thesis, The University of Bath, 2006.

[26] D. J. Cleaver, Z. Wang, and I. Gursul, Bifurcating flows of plunging aerofoils at high Strouhal numbers, Journal of Fluid Mechanics **708**, 349 (2012).

[27] D. E. Calderon, D. J. Cleaver, I. Gursul, and Z. Wang, On the absence of asymmetric wakes for periodically plunging finite wings, Physics of Fluids **26**, 349 (2014).

[28] J. J. Charonko, and P. P. Vlachos, Estimation of uncertainty bounds for individual particle image velocimetry measurements from cross-correlation peak ratio, Measurement Science and Technology **24**, 065301 (2013).

[29] R. W. Heiland, KLTOOL: a mathematical tool for analyzing spatiotemporal data, Arizona State University, 1992.

[30] B. W. van Oudheusden, F. Scarano, N. P. Hinsberg, and D. W. Watt, Phase-resolved characterization of vortex shedding in the near wake of a square-section cylinder at incidence, Experiments in Fluids **39**, 86 (2005).

[31] K. D. Frampton, M. Goldfarb, D. Monopoli, and D. Cveticanin, Passive Aeroelastic Tailoring for Optimal Flapping Wings, Fixed and Flapping Wing Aerodynamics for Micro Air Vehicle Applications, edited by Mueller, T. J., Progress in Astronautics and Aeronautics, Vol. 185, AIAA, Reston, VA, 2001, pp. 473–482.

[32] S. Heathcote, and I. Gursul, Flexible Flapping Airfoil Propulsion at Low Reynolds Numbers, AIAA Journal, **45**, 1066 (2007).

[33] Y. Qian, Z. Wang, and I. Gursul, Interaction of Quasi-Two-Dimensional Vortical Gusts with Airfoils, Unswept and Swept Wings, Experiments in Fluids, **63**, 124 (2022).

[34] D. E. Calderon, Z. Wang, I. Gursul, and M. R. Visbal, Volumetric measurements and simulations of the vortex structures generated by low aspect ratio plunging wings, Physics of Fluids **25**, 067102 (2013).

[35] N. Chiereghin, S. Bull, D. J. Cleaver, and I. Gursul, Three-dimensionality of leading-edge vortices on high aspect ratio plunging wings, Physical Review Fluids **5**, 064701 (2020).

[36] D. J. Cleaver, Z. Wang, I. Gursul, and M. R. Visbal, Lift enhancement by means of small-amplitude airfoil oscillations at low Reynolds numbers, AIAA Journal **49**, 2018 (2011).

[37] Y. Qian, Z. Wang, and I. Gursul, *Interaction of Quasi-Two-Dimensional Vortical Gusts with Swept and Unswept Wings*, AIAA 2021-1935, (AIAA Scitech Forum, 2021).

[38] W. R. Sears, Some aspects of non-stationary airfoil theory and its practical application, J. Aeronaut. Sci. **8**, 104 (1941).

[39] T. Theodorsen, General theory of aerodynamic instability and the mechanism of flutter, NACA Tech. Rep. 496, 1935.